

# Bridging the gap between SLSNe and SE-SNe

## Multi-wavelength analysis of the SLSN-Ib SN 2024jlc

A. Simongini<sup>1,2\*</sup>, F. Acero<sup>3,4</sup>, M. Imbrogno<sup>5,6,1</sup>, J. L. Wise<sup>7</sup>, J. Sollerman<sup>8</sup>, S. Schulze<sup>9</sup>, N. Paul M. Kuin<sup>10</sup>, T. X. Chen<sup>11</sup>, C. Fremling<sup>12,13</sup>, A. Gangopadhyay<sup>8</sup>, M. M. Kasliwal<sup>11</sup>, R. R. Laher<sup>11</sup>, Z. McGrath<sup>7</sup>, D. A. Perley<sup>7,14</sup>, J. N. Purdum<sup>12</sup>, N. Rehemtulla<sup>15,9,16</sup>, R. M. Rich<sup>17</sup>, and R. Riddle<sup>12</sup>

(Affiliations can be found after the references)

Received XX YY, ZZZZ; accepted xx yy, zzzz

### ABSTRACT

The Type I super-luminous supernova SN 2024jlc (ZTF24aapadbb) exploded on the 25th of May 2024 at  $z = 0.039$ . Being the closest supernova of this class discovered in recent years and one of the closest ever, represented a rare opportunity to study in detail this type of objects. We performed a multi-wavelength analysis, spanning ten orders of magnitude in frequency, including optical/UV photometry and spectroscopy, soft and hard X-rays, and high-energy  $\gamma$ -rays. We characterized the event as a slow-evolving and He-rich supernova, with one of the lowest peak luminosities reported for a super-luminous event  $M_g \sim -19.37$  mag, and a light curve evolution compatible with both circumstellar interaction and magnetar spin-down models, with noticeable contribution from  $^{56}\text{Ni}$  decay. No significant excess was found in the soft and hard X-ray bands, for which we provide upper-limits on the flux. Additionally, we analyzed two years of *Fermi*-LAT data, from which we report an intriguing hint of a  $\gamma$ -ray signal at the  $\sim 3.6\sigma$  level, although no firm detection can be claimed. The gamma to optical efficiency ratio,  $\eta = 0.38$ , is suggestive of the presence of a central-engine scenario, similar to SN 2017egm. Our analysis suggests that SN 2024jlc could bridge the gap between SLSNe and classical stripped-envelope supernovae. While still poorly populated, this bridge could consist of all SLSN-Ib supernovae, with the key difference residing in the powering mechanism.

**Key words.** supernovae: general – supernovae: individual SN 2024jlc

### 1. Introduction

Super-luminous supernovae (SLSNe) defy the standard models of stellar explosions, significantly outshining normal thermonuclear and core-collapse supernovae (CCSNe). Mimicking the standard spectral classification scheme of CCSNe, all SLSNe can be classified based on the presence (SLSN-II) or absence (SLSN-I) of clear hydrogen features. Recently, helium has also been identified in the spectra of an increasing number of SLSN-I (e.g., Yan et al. 2020), suggesting a further sub-classification into SLSN-Ib and SLSN-Ic, based on the presence and absence of helium, respectively. Although the broad and often diverse properties exhibited by SLSN-I challenge the definition of a unified model, luminosities exceeding  $M \sim -20$  mag and the presence of spectral O II features have been identified as key diagnostics for recognizing a super-luminous event (e.g., De Cia et al. 2018; Chen et al. 2023a; Gomez et al. 2024). However, the discovery of several less luminous objects ( $-20 \leq M \leq -19$ ) raises the question of whether the canonical definition should be revised. These objects, also referred to as luminous supernovae (LSNe; Gomez et al. 2022), exhibit a broad diversity of features, with some resembling normal SLSNe in terms of spectral sequence and diffusion time, and others being more similar to normal stripped-envelope supernovae (SE-SNe), namely Type Ib, Ic, and Ic-BL. The key difference appears to be related to the powering mechanism. Normal SE-SNe are mainly powered by radioactive decay of Fe-group elements and, in some cases, can also have a contribution from the shock interaction between the ejecta and a circumstellar medium (CSM). On the other hand,

while CSM interaction can still account for the properties of some events (e.g., Wheeler et al. 2017; Zhu et al. 2023; Chen et al. 2023b), the preferred powering mechanism for SLSN-I is the spin-down of a rapidly rotating young magnetar. In some cases, both mechanisms may contribute (see for a review e.g. Howell 2017; Gal-Yam 2019; Inserra 2019; Moriya 2024).

Helium is typically absent from SLSN-I ejecta, or appears in a too limited quantity to form detectable spectral features (i.e. Kumar et al. 2025a). Only a few events have been claimed to show distinguishable helium features<sup>1</sup> (Yan et al. 2020; Terreran et al. 2020; Gomez et al. 2022; Zhu et al. 2023; Kumar et al. 2025b,a; Fiore et al. 2026). The majority of these events (with the only exception of SN 2017egm, SN 2021bnw, SN 2024ahr and SN 2024rmj) exhibits a relatively low peak luminosity, with a cut at  $M_g \leq -20.2$ . Apart from a few cases, they exhibit broad light curves, with high diffusion times and large ejecta masses (i.e.  $\geq 10 M_\odot$ ), although the velocity of the ejecta remains relatively low. Moreover, some of them show noticeable contribution from  $^{56}\text{Ni}$  decay (Gomez et al. 2024), with some of them having  $M_{\text{Ni}} \geq 1 M_\odot$ . Within the magnetar powering scenario, they tend to prefer slower spin periods than normal SLSNe, with average magnetic field intensities, a difference that can account for the low observed luminosity (Gomez et al. 2022). However, as pointed out by Chen et al. (2023b), some of these objects clearly prefer a CSM+ $^{56}\text{Ni}$  powering model and show light curve undulations. Although the true origin of such undulations is still

<sup>1</sup> To date: SN 1991D, SN 2003L, PTF10hgi, SN2017egm, SN 2018beh, SN 2018fcg, SN 2018kyt, SN 2019hge, SN 2019gam, SN 2019kws, SN 2019obk, SN 2019unb, SN 2020qef, SN 2021bnw, SN 2024ahr, SN 2024rmj.

\* E-mail: andrea.simongini@inaf.it

under debate, they proposed ejecta-CSM interaction as a possible solution, as well as ejecta clumpiness and changes in opacity. Interestingly, all these events show an early-time blue continuum and, except for SN 2017egm and SN 2024rmj, they do not exhibit obvious spectral W-shaped features. These O II features around 4200 and 4450 Å are considered a key spectral hallmark of SLSNe, distinguishing them from SNe Ic (Quimby et al. 2018). Gomez et al. (2022) suggested that the absence of these lines could result from low temperatures that prevent sufficient ion excitation at early times. However, as also noted by Chen et al. (2023b), the early-phase temperatures are in fact quite high, indicating that the lack of these features must have a different origin. Mazzali et al. (2016) proposed that the W-shaped features arise from excitation powered by magnetar spin-down, which would further support CSM interaction as the dominant powering mechanism in some cases. Lastly, SLSNe tend to prefer low mass host-galaxies ( $M \leq 10^9 M_\odot$ ), high star-formation rates and low local metallicities ( $\leq 0.5$  solar), with some exceptions (Gal-Yam 2019).

Owing to the extraordinary optical brightness, SLSNe have been the focus of extensive multiwavelength observational campaigns. Past observations indicate that these events tend to be faint in the other regions of the electromagnetic spectrum, with only a few that have been detected beyond optical.

X-ray observations were performed for over 30 SLSNe (Ofek et al. 2013; Levan et al. 2013; Inserra et al. 2017; Bhimbhakdi et al. 2018; Margutti et al. 2018), yet only three have been tentatively detected. X-ray emission occurs when the optical photons are up-scattered by the electrons accelerated in the shock front. The inverse Compton (IC) scattering mechanism is considered the primary driver of X-ray emission in young SNe and SLSNe, although thermal Bremsstrahlung can dominate at early times in cases of dense CSM environments like those seen in Type II<sub>n</sub> SNe. Past observations tend to favor the first scenario as dominant at around peak luminosity, suggesting the presence of a central engine rather than strong CSM interaction (e.g. Margutti et al. 2018), although the presence of a very thin layer of dense CSM around the exploded star could not be ruled out entirely. This highlights how significant the powering mechanism behind optical light curves can shape the emission at different wavelengths.

Another possible signature for CSM-interaction or magnetar spin-down is the emission in  $\gamma$ -rays. Potential  $\gamma$ -ray emission was searched for a population of more than 200 SLSNe in the energy range between 500 MeV and tens to hundreds of GeV (Renault-Tinacci et al. 2018; Crnogorčević et al. 2026). Two of these events were also observed at above TeV energies (Acharyya et al. 2023). No significant excess was found for any of these SNe except for SN 2017egm, which independent analyzes support as a strong candidate with  $\gamma$ -ray emission powered by magnetar spin-down (Li et al. 2026; Acero et al. 2026; Crnogorčević et al. 2026). Bright  $\gamma$ -ray emission has been predicted to arise both in the CSM-interaction and the magnetar spin-down models (e.g. Murase et al. 2011, 2015). In the CSM-interaction scenario, collisionless shocks following the interaction between the fast-moving ejecta and the slow CSM lead to efficient cosmic-ray acceleration and non-thermal radiation, from radio to  $\gamma$ -rays. This scenario is likely responsible for the evidence of radio emission from some SLSNe (Eftekhari et al. 2019; Margutti et al. 2023). Alternatively, the energy injection from a fast rotating magnetar into the SN ejecta may induce strong synchrotron and IC radiation, appearing a few months to years after the explosion (Kasen & Bildsten 2010; Vurm & Metzger 2021). Both models predict strong attenuation at high ener-

gies in the first days to weeks due to pair-production processes established between  $\gamma$ -rays and the optical photons of the photosphere, namely  $\gamma$ - $\gamma$  absorption (Brose et al. 2022), and between  $\gamma$ -rays and the dense field of nuclei and thermal electrons within the ejecta, namely Bethe-Heitler (BH) absorption (Crnogorčević et al. 2026). The key difference between the two models is that, in the CSM-interaction scenario, the  $\gamma$ -ray flux is confined to the brief period when the ejecta encounter the CSM. If that material is restricted to small radii around the exploding star, the resulting  $\gamma$ -rays may be fully suppressed by pair production, leaving no detectable signal. In contrast, the magnetar model is not limited by external conditions, so particle acceleration, and thus  $\gamma$ -ray production, can occur continuously without significant absorption.

Here, we present a multi-wavelength analysis of SN 2024jlc (ZTF24aapadbb), one of the closest and least luminous SLSNe-I discovered to date. The paper is laid out as follows: we present the event and its host-galaxy in Sect. 2 and report our observations in Sect. 3. Section 4 and Sect. 5 are entirely dedicated to the characterization of the optical light curves and spectra. In Section 6 we model our X-rays and  $\gamma$ -rays data. Finally, we discuss our results in Sect. 7, and our conclusions are reported in Sect. 8.

## 2. Discovery and host galaxy

SN 2024jlc was discovered on 28 May 2024 at 06:14:51 UTC by the Zwicky Transient Facility (ZTF; Bellm et al. 2019; Graham et al. 2019; Masci et al. 2018; Dekany et al. 2020) as ZTF24aapadbb with a discovery magnitude of  $g = 19.39$ , at coordinates RA(J2000) =  $15^{\text{h}}21^{\text{m}}58.812^{\text{s}}$ , DEC(J2000) =  $+62^{\text{d}}48^{\text{m}}22.69^{\text{s}}$  (Sollerman et al. 2024). SN 2024jlc was initially classified as a SN Ib at redshift  $z = 0.049$  (Pérez-Fournon et al. 2024), and later as a SLSN-I at redshift  $z = 0.039$  (Wise et al. 2024)<sup>2</sup>. The last non-detection is reported on 25 May 2024 at 09:14:58 UTC. Searching deeper into the ZTF forced photometry we found that the first detection happened on 25 May 2024 at 04:56:30 UTC (MJD 60455.21) with a discovery magnitude of  $g = 20.15 \pm 0.17$ . We adopt this time, hereafter  $t_0$ , as the reference epoch of explosion throughout the paper.

The SN is associated with the Panoramic Survey Telescope and Rapid Response System (Pan-STARSS, PS1; Flewelling et al. 2020) galaxy with id = 183362304927039129, centered at RA(J2000) =  $15^{\text{h}}21^{\text{m}}58.178^{\text{s}}$ , DEC(J2000) =  $+62^{\text{d}}48^{\text{m}}25.16^{\text{s}}$  and with a reported luminosity of  $m_r \sim 18.47$ . If the association is confirmed, SN 2024jlc would be offset by  $4.9'' \approx 4.3$  kpc from the host galaxy center. To analyze the integrated host properties, we retrieved science-ready co-added images from the PS1-DR1 (Chambers et al. 2016) and the re-processed images from the *Wide-field Infrared Survey Explorer* (WISE; Wright et al. 2010) from the unWISE archive (Lang 2014). The unWISE images include data from the NEOWISE Reactivation mission (Mainzer et al. 2014; Meisner et al. 2017) through Year 6/7. We measured the brightness with the LAMBDA (Lambda Adaptive Multi-Band Deblending Algorithm in R; Wright et al. 2016) and utilize tools developed by Schulze et al. (2021) to measure the input parameters for LAMBDA. See Table A.1 for the measurements. We model the host spectral energy distribution (SED) with the software package Prospector version 1.4 (Johnson et al. 2021). Prospector uses the Flexible Stellar

<sup>2</sup> Note that the two estimates were obtained using two different techniques: Pérez-Fournon et al. (2024) used a template-matching software, while Wise et al. (2024) estimated it directly from the spectrum using host emission lines, as we did in this work.

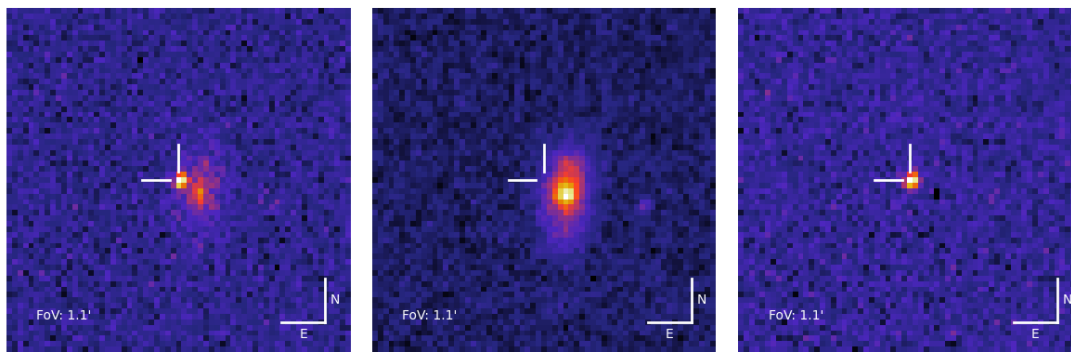


**Fig. 1.** Detection of SN 2024jlc on ZTF g-band images. (Left): target image from 28 May, 2024; (middle): deep pre-explosion reference image; (right): difference image post-explosion.

Population Synthesis (FSPS) code (Conroy et al. 2009) to generate the underlying physical model and `python-fsps` (Foreman-Mackey et al. 2014) to interface with python. We assume a parametric star-formation history of the form  $t \times \exp(-t/\tau)$ , where  $t$  is the age of the SFH episode and  $\tau$  is the  $e$ -folding timescale, the Chabrier (2003) initial mass function, the Calzetti et al. (2000) attenuation model, and the Byler et al. (2017) model for the ionized gas contribution. The priors were set similar to those in Schulze et al. (2021). All parameters were inferred in a Bayesian way by sampling the posterior probability functions with the dynamic nested sampling package `dynesty` (Speagle 2020) version 2.1.4. We infer a galaxy mass of  $\log(M_*/M_\odot) = 9.25^{+0.15}_{-0.18}$  and a star-formation rate of  $0.05^{+0.13}_{-0.05} M_\odot \text{ yr}^{-1}$ , albeit the lack of data blueward of the  $g$  band limits the constraints on the star-formation rate.

We collected one spectrum of the host-galaxy with the MMT-Binospec (Fabricant et al. 2019) at 335 days after the explosion. The MMT spectrum shows emission lines from the ionized gas in H II regions along the line of sight. Their luminosities and flux ratios allow to determine the metallicity of the gas in the star-forming regions, the metal enrichment and the level of attenuation. The MW-extinction corrected  $H\alpha$ - $H\beta$  flux ratios is  $\approx 3.02$ , marginally larger than the theoretically expected value of 2.86 for Case B recombination (Osterbrock & Ferland 2006). The nominal excess in the flux ratio translates to  $E_{\text{host}}(B-V) = 0.05 \pm 0.07$  mag, assuming the Calzetti attenuation model with  $R_V = 4.05$ . The attenuation-corrected  $H\alpha$  luminosity translates to a star-formation rate of  $0.010 \pm 0.002 M_\odot \text{ yr}^{-1}$  using Kennicutt (1998) and Madau & Dickinson (2014) to convert from the Salpeter IMF (assumed in Kennicutt 1998) to the Chabrier IMF (assumed in our galaxy SED modeling). We determine the metallicity of the gas in the star-forming region using the O3N2 and N2 diagnostics (Pettini & Pagel 2004) and the parameterizations from Curti et al. (2017). We measure a metallicity of  $0.50 \pm 0.03$  solar. The local metallicity is a bit lower than the expected galaxy metallicity based on the mass-metallicity relation (Andrews & Martini 2013), but consistent within errors.

### 3. Observations and data

We report observations of SN 2024jlc, spanning ten orders of magnitude in frequency, including UV, optical, soft and hard X-rays and high-energy  $\gamma$ -rays. All UV and optical data are reported in Table A.2 and Table A.3, while the X-rays data are given in Table A.4. The  $\gamma$ -ray data are publicly available on the Fermi-LAT database.

#### 3.1. Optical photometry

We obtained ZTF  $gri$  photometry using the ZTF forced-photometry service (Masci et al. 2018) via the ZTF Fritz marshal, an instance of SkyPortal (van der Walt et al. 2019; Coughlin et al. 2023). Also, we obtained photometry in the Sloan Digital Sky Survey (SDSS; Albareti et al. 2017)  $g$ ,  $r$ ,  $i$  and  $z$  filters with the IO:O photometer mounted on the Liverpool Telescope (LT; Steele et al. 2004). Images were processed using the `subphot_pipe`<sup>3</sup> image subtraction and PSF photometry pipeline, with PS1 reference images used for subtraction, and photometry measured using PSF fitting methodology relative to PS1 standards based on the technique outlined in Fremling et al. (2016). We retrieved data from the Asteroid Terrestrial-impact Last Alert System (ATLAS; Tonry et al. 2018; Smith et al. 2020; Shingles et al. 2021) in the  $c$  and  $o$  filters. These light curves range from  $t_0$  to  $t_0 + 452$  d and cover the rise, the peak and the decline phase in all filters. The  $g$ -band light curve peaks at  $t_{\text{max}} = 60504.43 \pm 2.64$  MJD (2024-07-13 10:23:09.442 UTC), indicating a rest-frame rise time of  $t_{\text{rise}} = 49.23 \pm 2.64$  d. This is similar to the rise times in the  $r$  band ( $50.02 \pm 2.42$  d), in the  $i$  band ( $49.64 \pm 3.31$  d) and in the  $o$ -band ( $51.49 \pm 0.44$  d). The rise time of SN 2024jlc aligns with the average of typical slow evolving SLSNe-I (i.e. 52 days; Inserra 2019).

#### 3.2. Optical spectroscopy

We collected 21 spectra of SN 2024jlc and one of its host galaxy (see Table A.3 for details). In particular, we collected 14 spectra with the Spectral Energy Distribution Machine (SEDM; Blagorodnova et al. 2018; Rigault et al. 2019; Kim et al. 2022).

We also obtained two spectra with the SPectrograph for the Rapid Acquisition of Transients (SPRAT; Piascik et al. 2014) at the LT using a blue-optimized setup, which were reduced using a custom python pipeline. This pipeline is based on the packages `lacosmic` (Van Dokkum 2001), `NumPy` (Van Der Walt et al. 2011), `SciPy` (Virtanen et al. 2020), and `Astropy` (Price-Whelan et al. 2022). Polynomial fits for sky subtraction and trace fitting, as well as the setting of the aperture sizes, were performed manually to optimize the signal to noise ratio. We corrected for airmass differences between the science and standard star exposures using Table 1 from La Palma Technical Note No. 31<sup>4</sup>. One spectrum was obtained with the KAST spectrograph at the Lick Observatory (Miller & Stone 1994). The

<sup>3</sup> [https://github.com/kryanhinds/subphot\\_pipe](https://github.com/kryanhinds/subphot_pipe)

<sup>4</sup> [https://www.ing.iac.es/Astronomy/observing/manuals/ps/tech\\_notes/tn031.pdf](https://www.ing.iac.es/Astronomy/observing/manuals/ps/tech_notes/tn031.pdf)

300/7500 grating (2.55 Å/pixel dispersion) was used for the red side, and the 600/4310 grism (1.02 Å/pixel dispersion) was used for the blue side. A slit width of 2.0" was used for all observations. The spectrum was reduced using the UCSC spectral pipeline<sup>5</sup> (Siebert et al. 2020), a custom data-reduction pipeline based on procedures outlined by Foley et al. (2003) and Silverman et al. (2012), utilizing the optimal one-dimensional spectral extraction algorithm from Horne (1986). We also observed SN 2024jlc with the Binospec instrument (Fabricant et al. 2019) installed on the 6.5 m MMT telescope at MJD 60791.39. Binospec was configured to use the 270 lines/mm grating, achieving wavelength coverage between 3820–9210 Å with  $R \sim 1340$ . The data are reduced using standard procedures implemented in the `pypeit` software package (Prochaska et al. 2020). Additionally, we collected two spectra with the Alhambra Faint Object Spectrograph and Camera (ALFOSC; Djupvik & Andersen 2010), and one with the Double Spectrograph (DBSP, Oke & Gunn 1982). Our spectra cover the time range from 13 to 337 days after the explosion and the wavelength range 3500 – 10500 Å. We estimate the redshift using the narrow  $H\alpha$  emission line in the host-galaxy, obtaining  $z = 0.0392 \pm 0.0058$ , similar to the previous estimation by Wise et al. (2024). Assuming a flat  $\Lambda$ CDM Universe with  $H_0 = 67.4 \text{ km s}^{-1} \text{ Mpc}^{-1}$ ,  $\Omega_m = 0.315$  and  $\Omega_\Lambda = 0.685$  (Planck Collaboration et al. 2020), we obtain a luminosity distance of  $D_L = 179.38 \pm 17.94 \text{ Mpc}$ , making SN 2024jlc one of the closest classified SLSNe-I to date, after SN 2018bsz (Anderson et al. 2018), SN 2017egm (Zhu et al. 2023), SN 2020wnt (Tinayanont et al. 2023) and SN 2019ieh (Dahiwalé et al. 2019). Consequently, we obtain a distance modulus of  $\mu = 36.27 \pm 0.22 \text{ mag}$ .

### 3.3. Swift-UVOT photometry

The observations of SN 2024jlc with the Neil Gehrels *Swift* space telescope, hereafter *Swift* (Gehrels et al. 2004), were triggered as a target of opportunity (P.I. T. Moore; target ID 16706) three non-consecutive nights in July 2024, before and after the peak of optical luminosity. The Ultra-Violet Optical Telescope (UVOT; Roming et al. 2005) took data with all six filters (w2, m2, w1, u, b, v), resulting in a total exposure time of 4885 seconds. UVOT photometry was processed using the standard `uvotsource` module (Poole et al. 2008; Breeveld et al. 2011) within the HEASOFT package for *Swift*-UVOT analysis, using CALDB 2023-12-08<sup>6</sup>. The complete photometry is reported in Table A.2.

### 3.4. Swift-XRT observations

The X-ray Telescope (XRT; Burrows et al. 2005) on board the *Swift* satellite took data in PC mode simultaneously to UVOT. The observations were conducted in an energy range of 0.3 – 10 keV for a total exposure of 4880 s. Data were reduced using the `xrtpipeline` and count rates were estimated with the `sosta` tool from the HEASOFT package. Fluxes were derived in the WebPIMMS portal. Assuming a photon spectral index of 2 and a Galactic hydrogen column density of  $N_H = 1.38 \times 10^{20} \text{ cm}^{-2}$  (Bekhti et al. 2016), we derived  $3\sigma$  flux upper limits (Table A.4) in the full energy band. Integrating over the full time range, we obtain a total absorbed flux upper limit of  $F_x \leq 0.838 \times 10^{-13} \text{ erg cm}^{-2} \text{ s}^{-1}$ , corresponding to a luminosity of  $L_x \leq 3.36 \times 10^{41} \text{ erg s}^{-1}$ . Owing to the vicinity of the event, despite the relatively

low exposure time, these upper limits are among the deepest for SLSNe-I in the range 0.3 – 10 keV, slightly above the possible detection of PTF12dam ( $L_x \sim 2 \times 10^{40} \text{ erg s}^{-1}$ ; Margutti et al. 2018) and the upper limits of SN 2017egm ( $L_x \sim 1.9 \times 10^{39} \text{ erg s}^{-1}$ ; Zhu et al. 2023).

### 3.5. Swift-BAT observations

During the *Swift* follow-up, the Burst Alert Monitor (BAT; Barthelmy et al. 2005) took data in survey mode. This mode allows the instrument to monitor the entire field of view for hard X-ray transients in the 15 – 150 keV band, collecting count-rate data in five-minute time bins. In case of a significant burst, the instrument switches to a photon-by-photon mode, specifically designed to localize and follow fast transients. BAT data are processed using the BATIMAGER software (Segreto et al. 2010). This software is specifically designed to perform image reconstruction and generate spectra and light curves of a source. Count rates on the position of the SN are estimated for one day of observation (60517 MJD) and for the full month of July 2024. We obtain  $(-2.63 \pm 1.48) \times 10^{-4} \text{ cts s}^{-1}$  and  $(-6.71 \pm 2.55) \times 10^{-5} \text{ cts s}^{-1}$  respectively. The statistical errors follow a Gaussian distribution at  $1\sigma$ . Subsequently, fluxes are derived from the WebPIMMS portal assuming the same properties as those used for the XRT observations and a power-law fit. We obtain absorbed fluxes upper limits of  $F_x \leq 9.06 \times 10^{-11} \text{ erg cm}^{-2} \text{ s}^{-1}$  and  $F_x \leq 1.56 \times 10^{-11} \text{ erg cm}^{-2} \text{ s}^{-1}$  corresponding to a luminosity upper limit of  $L_x \leq 3.49 \times 10^{44} \text{ erg s}^{-1}$  and  $L_x \leq 6.01 \times 10^{43} \text{ erg s}^{-1}$  respectively.

### 3.6. Fermi-LAT monitoring

High energy (MeV – GeV)  $\gamma$ -ray data were collected with the *Fermi*-Large Area Telescope (LAT) space telescope (Atwood et al. 2009). Because *Fermi*-LAT scans the entire sky approximately every three hours, the position of SN 2024jlc was within its field of view for almost 50% of the time. Data analysis was performed using the *Fermitools* version 2.4.0<sup>7</sup> and `fermipy` v1.4 packages (Wood et al. 2018), with standard models for Galactic (`gll_iem_v07.fits`) and isotropic diffuse emission (`iso_P8R3_SOURCE_V3_v1.txt`). To optimally handle the LAT point-spread function (PSF) strong energy dependence, we performed a summed PSF likelihood method. Specifically, events were simultaneously fit using the four PSF event types<sup>8</sup>, each corresponding to a different level of angular reconstruction quality, and the total likelihood was computed as the sum over these components. We used 4 components, of which three (PSF1, PSF2, and PSF3) in the 100 MeV – 1 GeV energy range with a zenith angle cut of  $< 90^\circ$ , and a single component above 1 GeV with all event types and a broader maximum zenith angle cut of  $105^\circ$ . The analysis was performed over a  $10^\circ \times 10^\circ$  region centered on the SN coordinates, using the latest release of the 4FGL-DR4 catalog as the baseline source model (Ballet et al. 2023). The details of the fitting procedure are similar to the one described in Sect. 2.3 of Acero et al. (2026).

To evaluate the significance of the  $\gamma$ -ray signal from the SLSN, we modeled a point source at the optical coordinates using a power-law spectrum,  $E^{-\Gamma}$ , with a fixed spectral index of  $\Gamma = 2$ . We assessed the statistical significance of this signal using the likelihood ratio test statistic, defined as  $\text{TS} = 2(\ln \mathcal{L}_1 - \ln \mathcal{L}_0)$ ,

<sup>7</sup> <https://fermi.gsfc.nasa.gov/ssc/data/analysis/documentation/>

<sup>8</sup> [https://fermi.gsfc.nasa.gov/ssc/data/analysis/documentation/Cicerone/Cicerone\\_Data/LAT\\_DP.html](https://fermi.gsfc.nasa.gov/ssc/data/analysis/documentation/Cicerone/Cicerone_Data/LAT_DP.html)

<sup>5</sup> [https://github.com/msiebert1/UCSC\\_spectral\\_pipeline](https://github.com/msiebert1/UCSC_spectral_pipeline)

<sup>6</sup> <https://swift.gsfc.nasa.gov/caldb/>

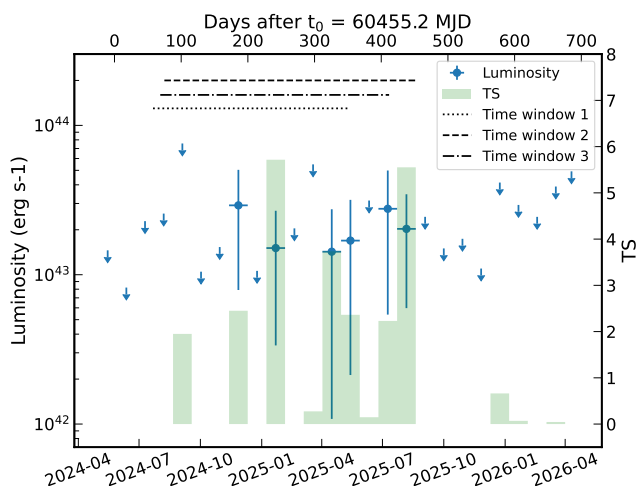


**Fig. 2.** *Fermi*-LAT  $\gamma$ -ray light-curve of SN 2024jlc between April 2024 and April 2026 showing both the  $\gamma$ -ray energy flux and the TS in every monthly time bins. Upper-limits at a 95% confidence level are given for time bins with significance  $TS < 2$ . The time integration windows discussed in Sect. 6.2 are also represented, each representing a different set of parameters: model-independent (time window 1), CSM+ $^{56}\text{Ni}$  model (2), and magnetar spin-down model (3).

where  $\mathcal{L}_0$  and  $\mathcal{L}_1$  represent the likelihoods of the background-only and source-plus-background hypotheses, respectively.

Results are presented and discussed in Sect. 6.2. To put these results in context of the global time evolution of the  $\gamma$ -ray signal, we extracted a light-curve with monthly time bin keeping the diffuse background normalizations fixed to the best-fit value of the full time period. In order to account for source variability other than our target in the region, the normalization was set free for any source reaching  $TS > 16$  in any time bin. The resulting  $\gamma$ -ray light-curve is presented in Fig. 2.

## 4. Light curve analysis

### 4.1. Light curve evolution

The optical photometric evolution of SN 2024jlc is shown in Fig. A.1. Every magnitude is expressed in the AB standard photometric system. Light curves are analyzed with CASTOR (Simongini et al. 2024, 2025b), which applies Gaussian processes to smoothly interpolate data with no prior information. We adopt a foreground Galactic extinction of  $E(B - V) = 0.0182$  mag (Schlegel et al. 1998; Schlafly & Finkbeiner 2011), assuming the  $R_V$  values from McCall (2004). Absolute magnitudes are obtained after correcting for foreground extinction, host extinction (see Sect. 2) and K-correction.

We obtained a maximum absolute magnitude of  $M_{g,\text{peak}} = -19.37 \pm 0.22$  and  $M_{r,\text{peak}} = -19.39 \pm 0.22$ , similar to the first rough estimates from Wise et al. (2024) who reported  $M_g \sim M_r \sim -19.2$  at 49 days after discovery. Similarly, we obtained  $M_i = -19.28 \pm 0.23$ ,  $M_z = -19.32 \pm 0.22$  and  $M_o = -19.33 \pm 0.22$ , where the overall uncertainty is dominated by the uncertainty in the distance estimate. The low cadence of *Swift*-UVOT observations prevent a clear estimate of the peak of luminosity in any of its bands, although the observations were performed very close to the *g*-band maximum. Therefore, we obtain maximum absolute magnitude lower limits of  $M_u \leq -18.73$ ,  $M_b \leq -19.53$  and  $M_v \leq -19.63$  in the near-UV bands and  $M_{w2} \leq -17.32$ ,  $M_{m2} \leq -17.45$  and  $M_{w1} \leq -17.95$  in

the UV bands. These values are generally under-luminous when compared to other SLSNe and seem more similar to the higher end of Type Ic-BL events, suggesting that SN 2024jlc could be a transitional event between the two classes.

Using the *griz* interpolated light curves we estimated an average rise rate between  $t_0$  and  $t_{\text{max}}$  of  $0.058 \pm 0.004$  mag  $\text{d}^{-1}$ , with *g* being the fastest to rise ( $49.23 \pm 2.64$  d) and *z* the slowest ( $52.84 \pm 4.12$  d). After, between the peak and day 80, the *g* band exhibits a steep decline of  $0.049 \pm 0.003$  mag  $\text{d}^{-1}$ , although the *rzi* light curves decrease more slowly, with an average of  $0.018 \pm 0.07$  mag  $\text{d}^{-1}$ . Then, between 80 and 150 days after the explosion, the decline is halted. During this time window, especially in the *g*, *r* and *o* bands, the light curve is almost flattened, with a global rate of  $0.004 \pm 0.002$  mag  $\text{d}^{-1}$ . This behavior can be observed at the same time with different instruments and in different filters. Afterwards, the luminosity starts dropping again, with a rate of  $0.013 \pm 0.002$  mag  $\text{d}^{-1}$ , measured between 200 and 400 days post-explosion. This late-time evolution is consistent with a  $^{56}\text{Co}$  nuclear decay-powered model, and it does not show the typical magnetar-powered tail as discussed in Inerra et al. (2013).

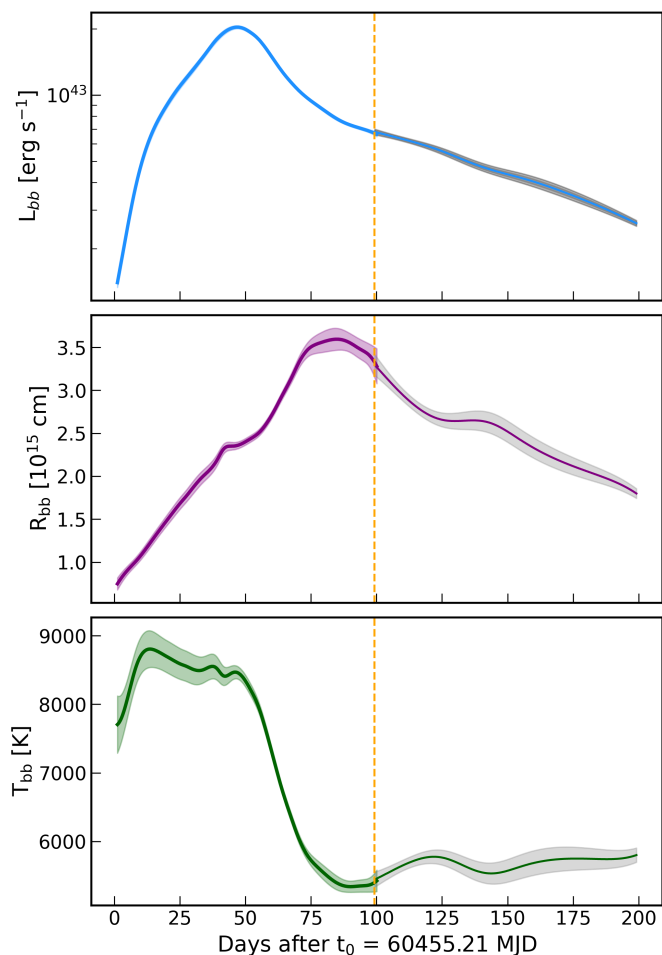
### 4.2. Color evolution

Figure A.1 presents the  $(g - r)$  color evolution of SN 2024jlc. Whereas the *Swift*-UVOT data are sparse and do not allow for a clear reconstruction of the color evolution, the ZTF dataset has a dense cadence, enabling a detailed tracking of the color trend over the full observation time. The  $(g - r)$  color displays an almost linear reddening from the explosion up to the peak of luminosity, reaching a value of  $(g - r)_{\text{MW} + \text{HG}} = 0.02 \pm 0.03$  mag when accounting for host-galaxy and Milky Way extinction. This value is consistent within the uncertainties of peak  $(g - r)$  colors in the SLSN-I sample of Chen et al. (2023a), who found  $(g - r)_{\text{median}} = -0.03_{-0.11}^{+0.12}$  mag after host-galaxy correction and without K-correcting. Afterwards, the color shifts towards the blue. Finally, after  $\sim 90$  days, the color exhibits an almost linear reddening trend. The early-time UV excess also indicates a strong ultraviolet contribution at early phases, which rapidly diminishes after the peak.

### 4.3. Photospheric evolution

The evolution of the bolometric luminosity and the photospheric temperature and radius during the first 200 days after the explosion is shown in Fig. 3. Calculations are performed with the software *extrab01* (Thornton et al. 2024), which derives the relevant parameters fitting a black-body to the available data. Notably, *extrab01* interpolates the available light curves (including UV data) with Gaussian process techniques. However, the available time coverage of UV and near-UV filters does not allow a complete reconstruction of the bolometric luminosity, although the black-body is often suppressed in the UV due to line blanketing. Thus, we perform two separate fits: the first, between  $t_0$  and  $t_0 + 100$  d including all interpolated filters, and the second, after  $t_0 + 100$  d using only *griz* filters.

We obtain a peak luminosity of  $L_{\text{BB}} = (2.03 \pm 0.03) \times 10^{43}$  erg  $\text{s}^{-1}$ , corresponding to  $M_{\text{BB}} = -19.57 \pm 0.02$ . These values indicate that SN 2024jlc is rather under-luminous if compared to the general definition of SLSNe-I, which corresponds to a peak magnitude lower than  $-20$  and a peak luminosity higher than  $3 \times 10^{43}$  erg  $\text{s}^{-1}$  (Moriya et al. 2018; Moriya 2024). Finally,



**Fig. 3.** (Top panel): bolometric luminosity; (central panel): photospheric radius; (bottom panel): photospheric temperature. The vertical dashed line at  $t_0 + 100$  identifies the separation between the first fit (all filters) and the second fit (only *griz* filters).

the total radiated energy during the entire duration of the light curve is  $E = 1.34 \times 10^{50}$  erg.

The temperature rises to its peak of  $T_{\text{BB}} = 8806 \pm 269$  K during the first 15 days after the explosion due to the high UV contribution, and then decreases significantly to a minimum of  $T_{\text{BB}} = 5339 \pm 82$  K at day  $\sim 90$ . Afterwards, it remains almost constant, to then rise again at about 200 days, where the blackbody assumption is no longer valid due to the onset of the nebular phase. The photospheric radius grows almost linearly from  $R_{\text{BB}} = 1 \times 10^{15}$  cm during the first 90 days, reaching a peak of  $R_{\text{BB}} = 3 \times 10^{15}$  cm, then recedes back to the starting value in the next hundred of days. The corresponding value of photospheric velocity at  $t_{\text{max}}$  is  $v_{\text{phot}} = 5600 \text{ km s}^{-1}$ . This evolution is in line with the average for SLSNe-I reported by [Chen et al. \(2023a\)](#) and [Gomez et al. \(2024\)](#).

#### 4.4. Diffusion time and mass of the ejecta

The mass of the ejecta has been identified as a good diagnostic for distinguishing SLSNe from SE-SNe explosions. On average, assuming similar opacities, SLSNe tend to eject masses that are 2–3 times larger than those of SE-SNe ([Nicholl et al. 2015](#); [Chen et al. 2023a](#)), although there are a few exceptions ([Karamehme-](#)

[toglu et al. 2023](#)). Regardless of the powering mechanism behind the explosion, it is possible to evaluate the mass of the ejecta based on the diffusion time. We define the diffusion time as  $\tau_m \sim (\tau_{\text{rise}} + \tau_{\text{dec}})/2$ , where  $\tau_{\text{rise}} = t(L_{\text{peak}}/e)$  for  $t < t_{\text{max}}$  and  $\tau_{\text{dec}} = t(L_{\text{max}}/e)$  for  $t > t_{\text{max}}$ . Subsequently, the mass of the ejecta can be expressed as a function of the width of the light curves, adapting the equations from [Kasen & Bildsten \(2010\)](#) and [Inserra et al. \(2013\)](#), by:

$$M_{\text{ej}} = 7.7 \times 10^{-7} \left( \frac{\kappa}{0.1 \text{ cm}^2 \text{ g}^{-1}} \right)^{-1} \frac{v}{\text{km s}^{-1}} \left( \frac{\tau_m}{\text{days}} \right)^2 M_{\odot} \quad (1)$$

where  $\kappa$  is the opacity and  $v$  is the "scale velocity", which is assumed as the expansion velocity of the ejecta. Here, we use  $v = 9800 \text{ km s}^{-1}$  (see Sect. 5 for the derivation of this parameter). For SN 2024jlc we find  $\tau_{\text{rise}} = 16.2$  days,  $\tau_{\text{dec}} = 87.8$  days and consequently  $\tau_m = 52.02$  days. Alternatively, following [Chen et al. \(2023a\)](#), we define the rise time as the time interval between the peak luminosity and the time at which the luminosity reaches 10% of its peak value. In this case, we obtain  $\tau_{\text{rise}, 10\%} = 42.9$  days. When compared to other events (e.g. [Nicholl et al. 2015](#); [Chen et al. 2023a](#)), SN 2024jlc rise time is well within the mean distribution found by [Chen et al. \(2023a\)](#) for SLSNe-I,  $41.9 \pm 17.8$  days, and faster than SE-SNe. The decline time is larger than for most SLSNe, but still within the distribution, and significantly higher than any SE-SNe. For comparison, as of [Nicholl et al. \(2015\)](#), the SN Ic SN 2011bm has the longest decline, of 57.2 days. Nevertheless, the diffusion time is consistent with other SLSN-I slow-evolving events, such as SN 2007bi (58.3 days), PTF12dam (55.2 days) and PS1-11ap (61.6 days).

Assuming  $\kappa = 0.1 \text{ cm}^2 \text{ g}^{-1}$  we found  $M_{\text{ej}} = 20.4^{+37.8}_{-18.4} M_{\odot}$ . Note that the uncertainty is obtained by applying Eq. 1 with  $\tau_m = \tau_{\text{dec}}$  and  $\tau_m = \tau_{\text{rise}}$  for the high and low error respectively. Finally, assuming the model by [Arnett \(1982\)](#), we get the kinetic energy of the ejecta of  $E_k = 1.17^{+3.0}_{-0.1} \times 10^{52}$  erg. Note that additionally to the case with  $\kappa = 0.1 \text{ cm}^2 \text{ g}^{-1}$ , [Nicholl et al. \(2015\)](#) investigate the scenario with  $\kappa = 0.2 \text{ cm}^2 \text{ g}^{-1}$ . In this case, the values of the mass of the ejecta and the kinetic energy are all halved and can be used as lower limits.

Although accompanied with high uncertainty, this result suggests the massive nature of the progenitor of SN 2024jlc, yielding an ejected mass at the high end of the distribution shown by [Nicholl et al. \(2015\)](#). For instance, assuming a neutron star with  $M_{\text{NS}} \geq 1.2 M_{\odot}$  as the most probable outcome of the explosion, by assuming perfect conservation of mass and using the lower limit of the mass of the ejecta obtained with  $\kappa = 0.2 \text{ cm}^2 \text{ g}^{-1}$ , we set a conservative lower limit to the mass of the progenitor of  $M_{\text{pro}} \geq 11 M_{\odot}$ .

#### 4.5. On the powering mechanism

To investigate the powering mechanism behind the evolution of SN 2024jlc, we used the MOSFiT software ([Guillochon et al. 2018](#)), as it is largely used in the literature for SLSNe. In particular, we tested the `slsnni` and the `csnni` models, as CSM-interaction and magnetar spin-down are the most common scenarios for SLSNe, and the shape of the light curves suggest the tails to be powered by  $^{56}\text{Ni}$  decay. Results and priors for the parameters are reported in Table A.6 and Table A.5. In addition to the MOSFiT fit, we cross-checked our results for the magnetar model with REDBACK ([Sarin et al. 2024](#)). Results are reported in Table A.5 and Table A.6, respectively.

Figure 4 shows the final results of the fit. Note that, given the low cadence of UVOT data, we used only our *griz* light curves.

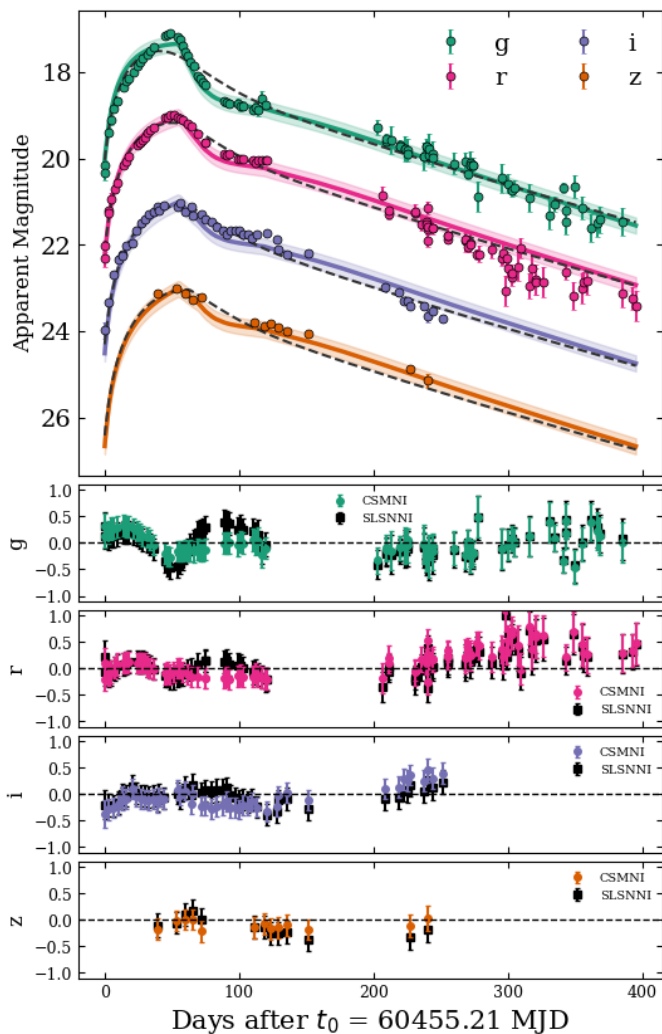


**Fig. 4.** Main panel: best fit of SN 2024jlc light curves (filled points, offset for clarity), using the *csmni* (solid color lines) and *slsnni* (dashed black lines) models from MOSFiT. Lower panels: normalized residuals for the two models expressed.

In both cases, we fixed the redshift, Galactic extinction and luminosity distance of the source, employing 5000 walkers to ensure a wide exploration of the parameter space. In general, both models well reproduce the shape of the light curves, with some caveats. The *csmni* model reproduces the rise and steep decline, as well as the following flattening. However, it fails in reproducing the *g*-band peak and the *r*- and *i*-bands late time decay. On the other hand, the *slsnni* model does not reproduce the undulation at around 80 days and the *g*-band rise, but yields a better fit of the *r*- and *i*-bands at late times. A similar underestimation of the *g*-band peak reconstruction was also noted by [Chen et al. \(2023b\)](#). To assess which model yielded the best fit, we evaluated the reduced chi-square for each pairs of filters and for the global fit. The *csmni* model yielded  $\chi^2/\text{d.o.f.} = (0.71, 1.24, 1.27, 0.67)$  for the *g*, *r*, *i*, and *z* bands respectively, while the *slsnni* model yielded  $\chi^2/\text{d.o.f.} = (1.12, 0.90, 0.64, 11.78)$ . When all filters are combined, the *csmni* yielded  $\chi^2_{\text{tot}}/\text{d.o.f.} = 1.03$  and the *slsnni*  $\chi^2_{\text{tot}}/\text{d.o.f.} = 1.00$ . This is suggestive of how both models are descriptive of SN 2024jlc light curves, and no mechanism can be confidently ruled out.

Notably, we performed additional tests changing the prior parameters for both models, and the presented realizations are the ones that yielded the lowest chi-square in both cases. In particular, we mostly focused on the mass of the ejecta, CSM mass, the nickel fraction, the magnetic field, and the magnetar spin period. We note that in both cases, better fits were achieved by minimizing the secondary power sources: *slsnni* preferring a weak magnetar field, while *csmni* preferring a low CSM envelope, leaning heavier on the nickel decay component. In both cases, intermediate values of  $M_{\text{ej}}$  are preferred, with too high or too low values degrading the first 100 days; similarly, higher nickel fractions are necessary to reproduce the tails. Specifically, in the *slsnni* model, no attempt resulted in a good reconstruction of the *g*-band peak and the undulation at 80 days, regardless of the prior exploration. Conversely, in the *csmni* model, increasing the CSM mass resulted in an artificial plateau at early phases.

For what concerns the luminosity tail, both models reproduce the overall behavior reasonably well, although they deviate slightly from the observed decay rate. In particular, the light curves exhibit a mean decline of about  $0.013 \text{ mag d}^{-1}$  (with some variation expected due to outliers and scatter in the data), whereas the *csmni* and *slsnni* fits yield decay rates of  $0.0097$  and  $0.0100 \text{ mag d}^{-1}$ , respectively. This deviation may point to partial  $\gamma$ -ray escape from the ejecta, a scenario that is plausible in the context of high expansion velocities and large  $^{56}\text{Ni}$  fractions, as proposed by [De Cia et al. \(2018\)](#). Assuming that the tail is completely powered by radioactive decay, we can use Arnett's model ([Arnett 1982](#)) to estimate the synthesized nickel mass. By fitting the luminosity tail, we obtained  $M_{\text{Ni}} = 0.60 \pm 0.02 M_{\odot}$ , which corresponds to  $f_{\text{Ni}} \sim 0.06 - 0.03$  depending on the opacity value. This result is in the high end of the distribution by [Gomez et al. \(2024\)](#), and indicates the relevant contribution from radioactive decay in powering the light curves.

## 5. Spectral analysis

We report spectroscopic observations of SN 2024jlc between 13 and 336 days after the explosion (see Fig. A.2). The early time spectra are characterized by a blue continuum and black-body temperatures of the order of 8000 K, in good agreement with the photospheric behavior shown in Fig. 3. This condition remains stable until  $\sim$  day 57 (i.e. 8 days after maximum), when the black body temperature starts dropping rapidly, reaching 5000 K in only ten days. In this short time window, the blue continuum fades almost entirely, marking the transition from photospheric to nebular phase.

In the following, we discuss the discernible features following the work by [Quimby et al. \(2018\)](#). Then, we tentatively match these features with known chemical features and, in particular, we discuss possible helium detections, which would make SN 2024jlc one of the few SLSNe-Ib known to date.

### 5.1. Spectral features

We investigate the spectral features of SN 2024jlc using the near-maximum spectrum taken at +48.71 d. In the work by [Quimby et al. \(2018\)](#), they divide SLSN-I spectra into two groups, based on the similarity with either SN 2011ke or PTF12dam. In agreement with the definition of PTF12dam-like events, when centering the spectrum on the emission feature at around 4600 Å, the emission feature at 5400 Å is blue-shifted. Broad emission features are clearly visible at  $\sim$  5000, 5800, 6100, 6500, 7800 and 8700 Å, thanks to the good signal-to-noise ratio in the optical

range. The emission features at 3600 and 4100 Å are less clearly discernible due to the low signal. Other features that are more prominent in PTF12dam-like spectra are the absorption dips at 5700 and 7600 Å. Adding to those, we find clear features at  $\sim 4750$ , 6200, 7000, 7350, 8300 and 9000 Å. The features at around 6500 Å and 7350 Å are telluric. Lastly, in general, the low signal-to-noise ratio in the bluest part of the spectra, does not allow for a clear identification of spectral features, although the smoothed spectra hint at possible features at  $\sim 3600$ , 3900 and 4400 Å.

We identify the ions responsible for the observed spectral features by comparing our spectra with those of other SLSNe-I, namely SN 2017egm (Zhu et al. 2023), SN 2019hge (Yan et al. 2020) and PTF10hgi (Yan et al. 2020). Our first spectrum was taken at 12.51 d post-explosion, when the photospheric temperature was already at its peak, entering a plateau that lasted for about 40 days. Consequently, the shape and the line intensity of all the early-time spectra taken during this time window remain very stable. The most discernible features, typical to SLSN objects, are the Ca II  $\lambda\lambda 3934$ , 3969 H&K doublet and the narrow (i.e. FWHM  $\sim 2000$ -3000 km s $^{-1}$ ) [Ca II]  $\lambda 7300$ . Less intense but still visible are the Fe II lines in the 4000-5000 Å range, the Na I  $\lambda 5890$  and the near-IR Ca II  $\lambda\lambda 8498$ , 8542, 8662 triplet. Strong metal lines, broad and intense start appearing clearly from 18.76 d post maximum, when the temperature has almost reached its minimum at 5000 K. The Ca II  $\lambda\lambda 3934$ , 3969 H&K doublet remains one of the strongest features, together with the near-IR Ca II  $\lambda\lambda 8498$ , 8542, 8662 triplet. Other species are now clearly discernible due to the disappearing of the blue continuum, such as the Ca II  $\lambda 3750$  and Fe II  $\lambda\lambda 4303$ , 4352, 5018, 5169, 5235, 5363. The spectra exhibit also strong Mg I  $\lambda 4571$  broad emission lines, with velocities of the order of 10000 km s $^{-1}$  and [Ca II]  $\lambda 7300$  with similar velocities, although contaminated by telluric lines. Similarly to SN 2017egm and SN 2019hge we note possible Na I  $\lambda 5890$  and Si II  $\lambda 6350$  features. Finally, oxygen lines are clearly visible, in particular [O I]  $\lambda 6300$  and O I  $\lambda 7774$ . Our last spectrum, at +286.89 d post-maximum, exhibits strong host-galaxy lines and broad metal features.

## 5.2. Helium lines

Two independent analyses performed using different spectra before the peak classified SN 2024jlc first as a SN Ib (Pérez-Fournon et al. 2024) and then as a SLSN-I similar to PTF10hgi (Wise et al. 2024). This motivated a deeper search for helium features in our spectral dataset.

We identify He I absorption features at  $\lambda\lambda 5876$ , 6678, 7065, 7281 with a similar blue-shift velocity  $\sim 9500$  km s $^{-1}$  at the time of the peak. The feature at  $\lambda 5876$  is the strongest of the four with a deep absorption dip. It first appears in our spectra at 13 days post explosion, with a blueshift velocity of 15200 km s $^{-1}$ , and it is identified throughout the entire evolution up to 120 days after the explosion. We fit the evolution of the velocity of this line with a power-law, obtaining  $v_{\text{peak}} = 9800 \pm 400$  km s $^{-1}$  at  $t_{\text{max}}$ . We assume this value as a reference velocity of the ejecta in our calculations.

The other three features are dimmer and not always above the noise level to be clearly identified, although they appear in several epochs. A direct comparison between the He I  $\lambda\lambda 5876$ , 7065, 7281 features of SN 2024jlc, SN 2017egm, SN 2019hge and PTF10hgi is shown in Fig. 5. Beyond spectral template matching with prototypical events, previous SLSNe-Ib were classified based on two key factors: (i) the presence of multiple He I fea-

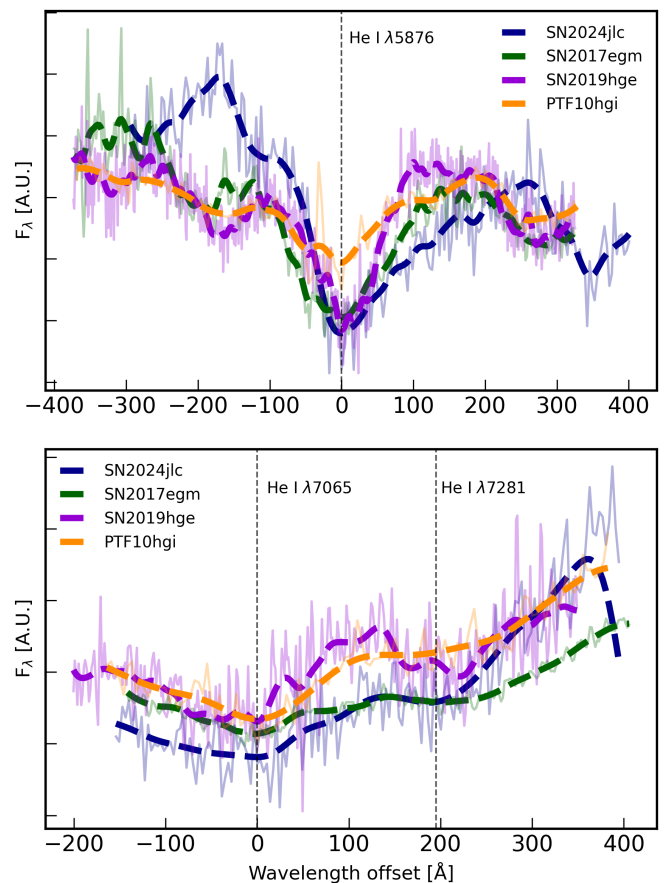


**Fig. 5.** Zoom-in around the He I  $\lambda 5876$  (upper panel) and He I  $\lambda\lambda 7065$ , 7281 (bottom panel) of different SLSNe-Ib. All the spectra are centered on the rest-frame value of the line, normalized to the highest flux and continuum-corrected. The normalization does not change between the two panels. We show: SN 2024jlc (71 days; this work), SN 2017egm (98 days; Zhu et al. 2023), SN 2019hge (67 days; Yan et al. 2020), PTF10hgi (105 days; Yan et al. 2020). Epochs are scaled to the epoch of maximum light.

tures across different epochs (see i.e. Yan et al. 2020; Zhu et al. 2023), and (ii) the identification of the near-IR He I  $\lambda 2.058$   $\mu\text{m}$  feature (see i.e. Yan et al. 2020; Kumar et al. 2025b), which is not contaminated by other elements. Despite the absence of near-IR data, that could reveal the He I  $\lambda\lambda 1.08$ , 2.05  $\mu\text{m}$  features (Kumar et al. 2025a,b), the detection of optical helium lines in multiple epochs of SN 2024jlc is already a strong indication of the existence of helium in the ejecta, making this object a new candidate for the SLSN-Ib class.

## 5.3. Nebular phase

Nebular spectroscopy can offer a view on the explosion's core and reveal the powering source. Nebular spectra can exhibit unique features as the innermost ejecta become directly observable. We collected one nebular spectrum of SN 2024jlc at 286 days post maximum. We found strong contribution from the [O I]  $\lambda 6300$  and [Ca II]  $\lambda 7300$  doublets, as well as Mg I  $\lambda 4571$  and O I  $\lambda 7774$  lines, as well as narrow host-galaxy features. Notably, the oxygen lines are much stronger than in the case of SN 2017egm and more similar to SLSN-I SN 2015bn (Nicholl et al. 2019) and the Type Ic-BL SN 2019odp (Schweyer et al.

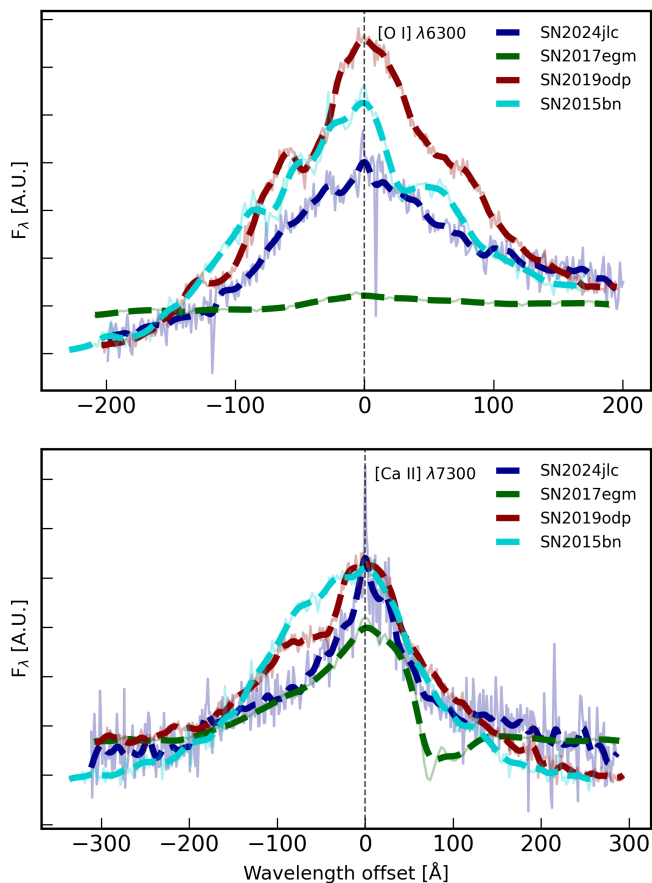


**Fig. 6.** Zoom-in around the [O I]  $\lambda 6300$  (upper panel) and [Ca II]  $\lambda 7300$  (bottom panel) of different objects. All the spectra are centered on the rest-frame value of the line, normalized to the highest flux and continuum-corrected. The normalization does not change between the two panels. We show: SN 2024jlc (286 days; this work), SN 2017egm (269 days; Zhu et al. 2023), SN 2019odp (138 days; Schweyer et al. 2025), SN 2015bn (350 days; Nicholl et al. 2019). Epochs are scaled to the epoch of maximum light.

2025; see Fig. 6). We estimate a calcium to oxygen luminosity ratio of  $L_{7300/6300} = 0.48 \pm 0.02$ . This ratio is sensitive to the core mass of the progenitor star, supporting the high-mass origin of the progenitor of SN 2024jlc (Karamahmetoglu et al. 2023). Our result is compatible with a previous estimation by Blanchard et al. (2026), who found  $L_{7300/6300} = 0.5 \pm 0.01$  using a spectrum taken at 257 days post maximum. For comparison, we estimate the same ratio with our second-last spectrum taken at 164 days post maximum, obtaining  $L_{7300/6300} \approx 1$ , although the transition to the nebular phase is not fully completed.

Another diagnostic useful for distinguishing between SLSNe and SE-SNe is the relative strength of the oxygen lines, quantified by the ratio  $L_{L7774/6300}$ . The oxygen line at  $7774 \text{ \AA}$  is ubiquitously detected in the sample of SLSNe studied by Blanchard et al. (2026), yielding  $L_{L7774/6300} \geq 0.15$ , whereas in SE-SNe this ratio is generally very small or consistent with zero. We obtain  $L_{L7774/6300} = 0.22 \pm 0.05$ , consistent with the previous estimate of  $L_{L7774/6300} = 0.24 \pm 0.01$  by Blanchard et al. (2026).

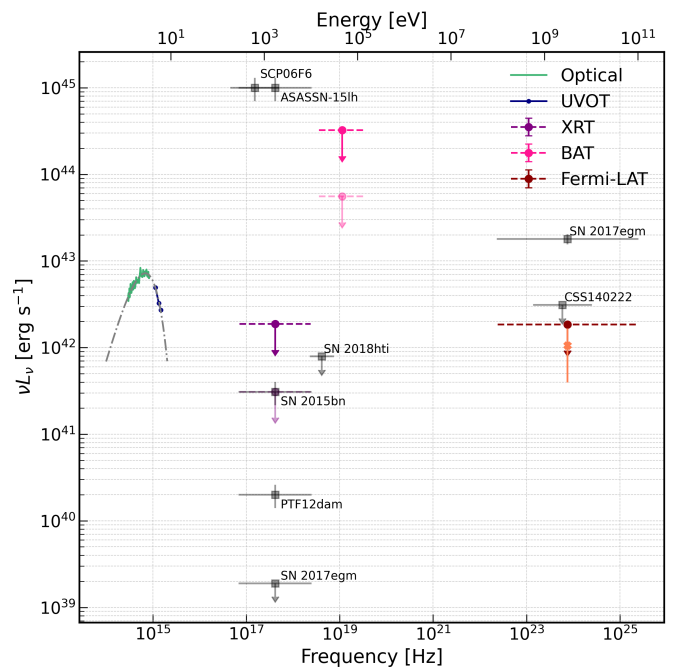


**Fig. 7.** Luminosity SED of SN 2024jlc near maximum light, from optical to high-energy  $\gamma$ -rays. A black-body is fit to the optical+UV data. For XRT and BAT, we plot both the night-wise upper limit (solid line) and the integrated upper-limit obtained by integrating over the entire observing period. For *Fermi*-LAT, we show both the upper-limit and the flux point as discussed in Sect. 6.2. As a comparison, we plot the published fluxes or flux upper-limits SCP06F6, ASASSN-15lh, SN 2018hti, PTF12dam, CSS140222 and SN 2017egm. Reference data are adapted from Levan et al. (2013); Margutti et al. (2017, 2018); Renault-Tinacci et al. (2018); Andreoni et al. (2022); Zhu et al. (2023); Acero et al. (2026).

## 6. On the multiwavelength SED

Figure 7 shows the multiwavelength SED of SN 2024jlc at +47 days after explosion. The SED includes data from optical to high-energy  $\gamma$ -rays, in the range  $10^{15} - 10^{25} \text{ Hz}$ . We compare our XRT, BAT and *Fermi*-LAT upper limits with published fluxes or flux upper limits of other SLSN-I events: SCP06F6, ASASSN-15lh, SN 2018hti, PTF12dam, CSS140222 and SN 2017egm (Levan et al. 2013; Margutti et al. 2017, 2018; Renault-Tinacci et al. 2018; Andreoni et al. 2022; Zhu et al. 2023; Acero et al. 2026).

### 6.1. X-rays: constraints on the CSM density

Assuming that the IC is the only source of X-ray radiation at  $t \sim t_{\text{max}}$ , we can use the formulation from Margutti et al. (2012) and Margutti et al. (2014) to constrain the density of the CSM using our XRT upper limits. In this model, the IC luminosity depends on the density structure of the ejecta and the CSM, the relativistic electron distribution, the mass of the ejecta, the kinetic energy and the bolometric optical luminosity and, in particular,  $L_{\text{IC}} \propto L_{\text{bol}}$ . We follow the same prescriptions as in Margutti et al. (2018), assuming a wind-generated medium with  $\rho_{\text{CSM}} \sim R^{-2}$ , a power-law electron distribution with  $p = 3$  and a fraction of post-shock energy into relativistic electrons of  $\epsilon_e = 0.1$ . Combining the parameters estimated in this work with the XRT upper-limit at +46 days, we constrain the mass-loss rate to wind velocity ratio of the progenitor star before the explo-

sion to  $\dot{M}/u_w \leq 1.05 \times 10^{-2} \frac{M_\odot}{\text{yr km}}$  with  $\kappa = 0.1 \text{ cm}^2 \text{ g}^{-1}$ . Similar results are obtained for each night of XRT observations. Additionally, by defining  $t_{\text{ref}}$  as the exposure weighted time of observation, equal to  $\approx 61$  days, we can leverage the integral upper-limit obtaining a final constrain of  $\dot{M}/u_w \leq 1.97 \times 10^{-3} \frac{M_\odot}{\text{yr km}}$  with  $\kappa = 0.1 \text{ cm}^2 \text{ g}^{-1}$  and  $\dot{M}/u_w \leq 2.91 \times 10^{-3} \frac{M_\odot}{\text{yr km}}$  with  $\kappa = 0.2 \text{ cm}^2 \text{ g}^{-1}$ . Unlike the case of SN 2015bn (Margutti et al. 2018), which has comparable explosion parameters and X-ray luminosity upper limits, our results do not rule out the possibility of a dense layer of CSM around the progenitor star, with the key difference being on the relative peak bolometric luminosity. Notably, our upper limits constrain a region confined within  $R_s \leq 6 \times 10^{15} \text{ cm}$  from the explosion site. Assuming a steady wind with  $u_w = 1000 \text{ km s}^{-1}$ , this translates to material expelled  $< 10$  years before the explosion.

## 6.2. Gamma-rays: hint of a signal and implications for the powering model

To have a physically motivated time integration window, we followed the prescription of Crnogorčević et al. (2026) to define the optimal search window for the GeV emission from SLSNe as  $[t_{\text{min}} = t_0 + 0.5t_{\text{BH}}(1+z), t_{\text{max}} = t_0 + 3t_{\text{BH}}(1+z)]$ , where:

$$t_{\text{BH}} \sim 91 \left( \frac{M_{\text{ej}}}{5M_\odot} \right)^{1/2} \left( \frac{v_{\text{ej}}}{6000 \text{ km s}^{-1}} \right)^{-1} \text{ d} \quad (2)$$

is the transparency time for pair production absorption. To define this time window, we adopted three sets of parameters for  $M_{\text{ej}}$  and  $v_{\text{ej}}$ :  $20.40 M_\odot$  and  $9800 \text{ km s}^{-1}$ , derived directly from model-independent analysis of the light curves and spectra (see Sect. 4.4 and Sect. 5),  $8.24 M_\odot$  and  $4815 \text{ km s}^{-1}$ , obtained from light-curve modeling under the assumption of a CSM+ $^{56}\text{Ni}$  powering mechanism (see Sect. 4.5), and  $8.47 M_\odot$  and  $5380 \text{ km s}^{-1}$  for the magnetar spin-down model. In the first case, we obtained a time window of 58.5 – 350.9 days after  $t_0$  and a corresponding  $\gamma$ -ray TS = 4.9 in the 100 MeV – 100 GeV energy range (time window 1 in Fig. 2). For the model-dependent cases, we estimated a time window of 75.6 – 453.8 and 68.6 – 411.8 days after  $t_0$  for the *csmni* and *slnni* values, obtaining a  $\gamma$ -ray signal of TS = 12.9 (time window 2 in Fig. 2), and TS = 7.01 (time window 3 in Fig. 2), respectively. Note that for one degree of freedom (power-law amplitude), these correspond to significance levels of  $\sim 2.2\sigma$ ,  $\sim 3.6\sigma$ , and  $\sim 2.6\sigma$ , respectively. While no firm detection can be claimed, a significance of  $\sim 3.6\sigma$  represents an intriguing hint, also noted by Crnogorčević et al. (2026)<sup>9</sup>. For model comparison, we derive a 95% confidence level integrated upper-limit over the range 100 MeV – 100 GeV of  $4.8 \times 10^{-13} \text{ erg cm}^{-2} \text{ s}^{-1}$  in the model dependent time window. As a hint of signal is present in the data, we also report the flux level of this putative signal  $2.7_{-1.0}^{+1.2} \times 10^{-13} \text{ erg cm}^{-2} \text{ s}^{-1}$ .

At the distance of SN 2024jlc, this flux corresponds to a  $\gamma$ -ray luminosity of  $L_\gamma = 1.06_{-0.45}^{+0.50} \times 10^{42} \text{ erg s}^{-1}$  (upper-limit of  $L_\gamma < 1.84 \times 10^{42} \text{ erg s}^{-1}$ ). Following the prescription of Crnogorčević et al. (2026), we define the GeV-to-optical efficiency  $\eta$  as the ratio of  $\gamma$ -ray to bolometric optical luminosity at the time when the ejecta become transparent,  $\eta \equiv L_\gamma/L_{\text{bol}}(t = t_{\text{BH}})$ . This yields  $\eta = 0.38$  (upper-limit of  $\eta < 0.67$ ), providing important implications for the powering mechanism behind SN 2024jlc.

<sup>9</sup> Notably, Crnogorčević et al. (2026) reported TS  $\sim 7$  in the range 50 – 645 days. However, as they also noted, this does not represent the optimal transparency window as it is not based on the definition of  $t_{\text{BH}}$ .

In the CSM-interaction scenario, the shock converts only a minor fraction of its kinetic energy into cosmic-rays, typically yielding  $\eta \sim 10^{-2} - 10^{-1}$ , as observed in novae (Cheung et al. 2022). Conversely, in a magnetar spin-down scenario, the efficiency can reach  $\eta \sim 1$  for weakly magnetized magnetar nebulae, where the spin-down power is converted equally between  $\gamma$ -rays and optical radiation (Vurm & Metzger 2021). However, in a highly magnetized scenario,  $\eta \ll 1$  because a larger fraction of the energy is emitted via synchrotron radiation in the X-ray bands, which is subsequently reprocessed into the optical regime. Among previous observations, only SN 2017egm yielded  $\eta \sim 1$  (Acero et al. 2026), while Crnogorčević et al. (2026) constrained  $\eta < 1.3 \times 10^{-3}$  for a population of 223 SLSNe-I.

Our results indicate a comparable  $\gamma$ -ray and optical luminosity, consistent with the magnetar spin-down scenario. This would also be the case even if the excess was not physical with the only caveat that our derived upper limit does not necessarily rule out either model. However, a difference of two orders of magnitude in efficiency is already a strong hint. While these findings may suggest that the tentative  $\gamma$ -ray emission of SN 2024jlc is driven by magnetar spin-down, they do not exclude the coexistence of alternative mechanisms contributing to the optical and X-ray emission, as suggested by our spectrophotometric analysis.

## 7. Discussion

We now summarize and discuss the observed properties of SN 2024jlc in a broader physical context. SN 2024jlc shares many similarities with normal SLSNe, although its relatively low luminosity and the detection of helium, set it apart, rising the question whether SN 2024jlc is rather a SE-SN of some kind. Quantitatively, we compare SN 2024jlc parameters with different samples (Taddia et al. 2015, 2019; Barbarino et al. 2021; Gomez et al. 2022; Karamehmetoglu et al. 2023; Gomez et al. 2024) and show the results in Fig. 8 and Fig. A.3.

### 7.1. On the similarities with SLSNe

SN 2024jlc appears to be a good match to the SLSNe-Ib class. Its light curves are broad, characterized by a high diffusion time and large ejecta masses. Both CSM+ $^{56}\text{Ni}$  and magnetar spin-down powering models provide a good fit to its light curves. The first scenario naturally explains the event's atypically low luminosity and is supported by the absence of the W-shaped features typically seen in other SLSNe, although the second scenario, with a slow magnetar spin-down, may as well explain the low luminosity. Finally, the spectra evolve from a featureless blue-continuum dominated to metal-rich, with noticeable He I features throughout the entire evolution. The nebular spectrum at 286 days post maximum exhibits strong [O I] and [Ca II] lines, and we estimated  $L_{7300/6300} = 0.48 \pm 0.02$ . This value is compatible with a previous estimation on a spectrum at 257 days performed by Blanchard et al. (2026). In their work, they collected the biggest sample of nebular spectra of SLSNe-I to date. They found that the  $L_{7300/6300}$  ratio is a good proxy for the level of ionization and that SLSNe-I have values spanning from  $\approx 0.2$  to  $\approx 6.2$  with a mean of  $\approx 1.4$ , with a decreasing trend over time that leads all events, apart from three outliers, to have a ratio below unity. They found that the general trend of SLSNe-I differs from SE-SNe, which show ratios below unity at all times, and that the difference may be pointing to the presence of a magnetar engine.

Finally, [Blanchard et al. \(2026\)](#) argued that the origin of the outliers, which exhibit an increasing level of ionization with time, may be caused by late-time interaction with CSM.

All observed properties of SN 2024jlc are consistent with the physical picture proposed by [Yan et al. \(2020\)](#) and [Chen et al. \(2023b\)](#), which can naturally explain the light curve shape and the presence of helium in the ejecta. In this interpretation, the progenitor star shed its hydrogen envelope long before explosion, preventing hydrogen signatures from appearing in the spectra, as seen in other stripped-envelope SNe. Helium, however, remained as a thin outer layer, and part of it was expelled shortly before core collapse, producing a denser He-rich CSM close to the star, surrounded by lower density regions. This would also explain the absence of narrow spectral lines, as these would disappear fast or, alternatively, these are suppressed by high temperatures that highly ionize the gas at early times. In this scenario, the excitation energy necessary to ionize helium would be reached by the classical transport of  $^{56}\text{Ni}$ , from the interior to the outer parts of ejecta.

[Chatzopoulos et al. \(2013\)](#) argued that instead of early-times narrow lines, the emission due to CSM interaction with a hydrogen-poor medium may appear as a late-time blue continuum or, as argued by [Blanchard et al. \(2026\)](#), by a high  $L_{7300/6300}$  ratio. Given the absence of both features, we exclude that SN 2024jlc light curves are powered by CSM interaction at late times.

## 7.2. On the similarities with SE-SNe

Among the (i)PTF sample of 220 SE-SN, [Karamehmetoglu et al. \(2023\)](#) estimated that a fraction of 13 per cent exhibits broad light curves, indicating large ejecta masses and high-mass progenitor stars. They presented a sample of 8 Type Ibc SNe<sup>10</sup> with shared properties that are uncommon to the rest of the population. These SNe exhibit rise times of the order of  $\sim 40$  days, higher than any other in the sample of Type Ibc events, and signs of undulations and/or multi-peak behavior. They are all connected with  $M_{\text{ej}} \gg 5M_{\odot}$ , while all previous Type Ibc samples had  $1 - 5M_{\odot}$  ([Taddia et al. 2019](#); [Barbarino et al. 2021](#)). Similarly, they all show higher nickel masses, with an average of  $M_{\text{Ni}} = 0.42 \pm 0.08 M_{\odot}$ , more than double than the typical value of  $0.2 \pm 0.14 M_{\odot}$ . Spectroscopically, they show typical Fe II, O I and Ca II lines, with velocities of the order of  $10^4 \text{ km s}^{-1}$ . The Type Ib SNe of the sample exhibit helium with high velocities, possibly blended with Na I $\delta$  at  $\lambda 5876$ , whereas the Type Ic show Si II and no signs of helium features. Their nebular spectra show strong [O I]  $\lambda\lambda 6300, 6364$  and [Ca II]  $\lambda\lambda 7319, 7324$ , with a relative luminosity ratio of  $L_{\lambda 7774/6300} \leq 0.81$ , indicating high-mass progenitors. Finally, they tend to prefer lower mass galaxies ( $\leq 10^{10} M_{\odot}$ ) with higher sSFR than normal SE-SNe, and more similar to the host galaxies of SLSNe-I and Type Ic-BL, and lower metallicity than 90 per cent of SE-SNe.

Given the strong similarities, it is natural to discuss whether SN 2024jlc should belong to this group of object. The many similarities demonstrate a similar host environment and explosion mechanism and similar progenitor stars. However, a strong limiting factor is given by the difference in luminosity. SN 2024jlc is  $\sim 1$  magnitude more luminous in every filter than the sample, which does not exhibit much scatter between single objects. Classifying SN 2024jlc as a Type Ibc with broad light curves would make it the most luminous SN of the class, with a dif-

ference greater than the one between SN 2024jlc and the least luminous SLSN-I. This may indicate that SLSNe-Ib are linked to broad SE-SNe, and the main difference could be found in the different powering mechanism: magnetar spin-down or CSM interaction with nickel decay in the first case and classical radioactive decay in the second.

Another possibility would be to link SN 2024jlc to the Type Ic-BL SNe, as they are the most luminous SE-SNe known, with some cases reaching even higher luminosities than SN 2024jlc ([Taddia et al. 2019](#)). In this case, however, the key limiting factor would be the broadness of the light curves. As also noted by [Chen et al. \(2023a\)](#), SNe Ic-BL exhibit narrower light curves, with a rise time lower than  $\tau_{\text{rise}, 10\%} \sim 25$  days. The brightest event from the sample of [Taddia et al. \(2019\)](#) shows a peak luminosity of  $M_{\text{g}} \sim -19.4$  (after color correction by [Chen et al. 2023a](#)), but a rise time of only 5 days. In this case, SN 2024jlc would not only represent one of the brightest Type Ic-BL ever discovered, but also the one with the broadest light curves.

## 7.3. Statistical comparison

We performed random forest classification with `scikit-learn` v1.9 ([Pedregosa et al. 2011](#)) to quantify the probability of SN 2024jlc to belong to a certain class given the estimated value of its parameters. As training samples, we used the data shown in Fig. 8 and Fig. A.3, focusing on the parameters that are common to every class: mass and velocity of the ejecta, kinetic energy, rise time, r-band peak magnitude, and mass of nickel. In total, the samples are constituted of 254 SLSNe-Ic ([Gomez et al. 2024](#)), 44 Type Ic ([Taddia et al. 2015](#); [Barbarino et al. 2021](#)), 30 Type Ic-BL ([Taddia et al. 2015, 2019](#)), 16 SLSNe-Ib ([Gomez et al. 2022, 2024](#); [Kumar et al. 2025b,a](#)), and 8 Type Ic with broad light-curves (Ic-BLC; [Barbarino et al. 2021](#); [Karamehmetoglu et al. 2023](#)). From these, we removed the SNe with missing parameters, for a total of 5 Type Ic and 2 Type Ic-BLC. To ensure a non-biased exploration towards the largely more populated class of SLSNe-Ic, we set `class_weight='balanced'`, and we ran the classifier for a total of 5000 estimators. We performed the classification for set of parameters of SN 2024jlc: first, using the model-independent values from Sect. 4.4, and then using the results from the `csnni` and `slnni` models reported in Table A.5 and Table A.6.

In all cases, SLSN-Ic is the class with the highest probability ( $\sim 40\%$ ), followed by SLSN-Ib ( $\sim 20\%$ ) and Ic-BLC ( $\sim 25\%$ ). Type Ic and Type Ic-BL ( $\leq 10\%$ ) are the least probable classes. If we exclude entirely the population of SLSNe-Ic from the random forest exploration, we obtain similar results, and the distance between SLSN-Ib and Ic-BLC from Types Ic and Ic-BL increases, as shown in Table 1. In particular, using model-dependent parameters, the probability associated to Type Ic-BLC increases to nearly 50%.

The parameters that weight the most are the r-band peak magnitude ( $\sim 35\%$ ), and the rise time ( $\sim 18\%$ ), which set the main difference between SE-SNe and SLSNe. The velocity of the ejecta ( $\sim 18\%$ ) weights mostly in downgrading the Ic-BL class, while the mass of nickel ( $\sim 10\%$ ), kinetic energy ( $\sim 9\%$ ) and mass of the ejecta ( $\sim 7.83\%$ ) have only a relative weight.

The lack of statistically well populated samples prevent us from giving a definitive conclusion, although these results may already represent a strong indication that SN 2024jlc is bridging SLSNe and SE-SNe. In all six realizations, the net separation between the SLSN and Ic-BLC samples from the normal SE-SNe ones represent a strong indication that SN 2024jlc is not

<sup>10</sup> Namely: PTF09dfk, PTF10inj, PTF11bov, PTF11mnb, PTF11rka, iPTF15dtg, iPTF16flq, iPTF16hgp.

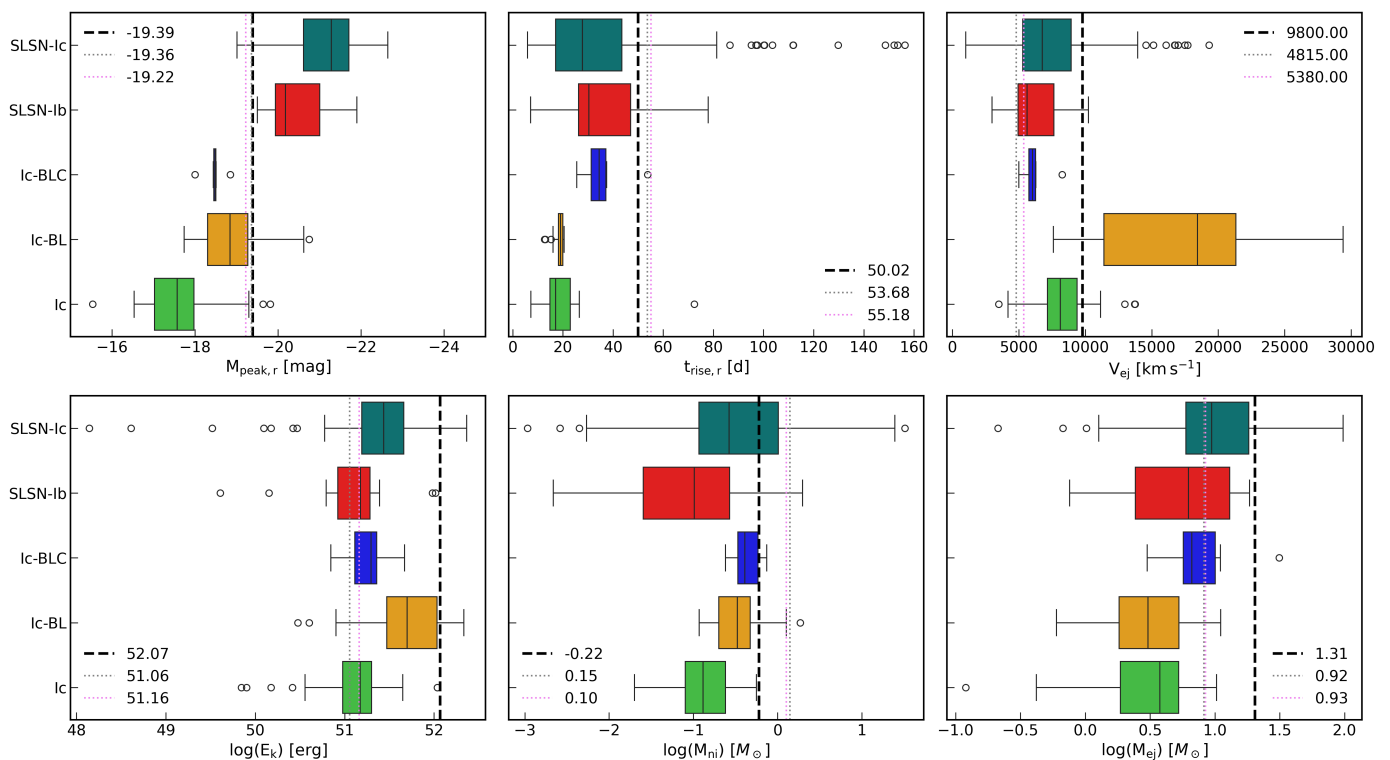


**Fig. 8.** Comparison of SN 2024jlc parameters with the distribution of the five samples: SLSN-Ic (teal), SLSN-Ib (red), Type Ic with broad light curves (blue), Type Ic-BL (orange), and Type Ic (green). We used three sets of SN 2024jlc parameters: model-independent (black dashed vertical lines), and the results from MOSFiT for the *csmni* (gray dotted vertical lines) and the *slsnni* (purple vertical dotted lines) models. In the last two cases, the r-band peak magnitude and rise time are directly extracted from the fitted curve of Fig. 4 for ensure self-consistency. The non-perfect reproduction of the peak (especially in the *slsnni* case) may weight on the final results.

**Table 1.** Results of random forest classification.

	SLSN-Ic	SLSN-Ib	Ic-BLC	Ic-BL	Ic
Model independent (%)	36.56	23.76	14.92	13.88	10.87
<i>csmni</i> (%)	38.38	23.16	26.18	3.42	8.87
<i>slsnni</i> (%)	34.38	19.31	34.31	3.15	8.84
Model independent (%)	–	34.85	32.00	21.46	11.68
<i>csmni</i> (%)	–	36.45	49.50	3.65	10.39
<i>slsnni</i> (%)	–	30.55	56.35	3.45	9.66

**Notes.** The probabilities are estimated for two sets of SN 2024jlc parameters: model independent refers to the estimations performed in Sect. 4.4, while *csmni* and *slsnni* refer to the parameters estimated using MOSFiT shown in Table A.5 and Table A.6. The second block represents the case without the SLSN-Ic sample.

a standard CCSN, while the boundary between SLSNe and Ic-BLC is less evident, if not for the very different magnitude peak.

## 8. Conclusions

We have presented a multi-wavelength analysis of SN 2024jlc, the closest SLSN-I discovered in recent years, and one of the closest ever. We included optical photometry and spectroscopy, covering the first year and a half after the explosion. Additionally, we estimated upper-limits on the X-ray flux and reported a possible hint of  $\gamma$ -ray signal. We highlight our major findings:

- i. SN 2024jlc is one of the least luminous SLSNe discovered to date, with a peak g-band absolute magnitude of  $-19.37 \pm 0.22$ .

- ii. SN 2024jlc light curves evolution are well fitted by both CSM+ $^{56}\text{Ni}$  and magnetar spin-down model.
- iii. From model-independent analysis, we found  $M_{\text{ej}} \approx 20 M_{\odot}$ ,  $E_{\text{k}} \approx 10^{52}$  erg and  $M_{\text{Ni}} \approx 0.6 M_{\odot}$ .
- iv. SN 2024jlc spectra exhibit a blue-continuum until  $\sim 12$  days after maximum, followed by a steep decrease in temperature and the emergence of strong metal features.
- v. SN 2024jlc spectra exhibit features of He I at  $5876 \text{ \AA}$ ,  $6678 \text{ \AA}$ ,  $7065 \text{ \AA}$  and  $7281 \text{ \AA}$ . The average expansion velocity at the peak of luminosity is  $9800 \pm 400 \text{ km s}^{-1}$ , in agreement with typical values for this class of objects.
- vi. From XRT and BAT observations we found  $L_{0.3-10 \text{ keV}} \leq 3.36 \times 10^{41} \text{ erg s}^{-1}$  and  $L_{15-150 \text{ keV}} \leq 6.01 \times 10^{43} \text{ erg s}^{-1}$ . These upper limits are used to constrain the mass-loss

to wind velocity ratio  $< 10$  years before the explosion to  $\dot{M}/u_w \leq 1.97 \times 10^{-3} \frac{M_\odot}{\text{yr km}}$ .

- vii. From *Fermi*-LAT observations we found an intriguing hint of a signal at a TS = 12.9 ( $\sim 3.6\sigma$  level), in line with previous results from Crnogorčević et al. (2026). This confirms SN 2024jlc as the SLSN with the highest TS ever found after SN 2017egm.
- viii. From *Fermi*-LAT observations we found  $L_\gamma = 1.06^{+0.50}_{-0.45} \times 10^{42} \text{ erg s}^{-1}$  (upper-limit of  $L_\gamma < 1.84 \times 10^{42} \text{ erg s}^{-1}$ ), corresponding to a GeV-to-optical efficiency of  $\eta = 0.38$  (upper-limit of  $\eta < 0.67$ ).

Our spectrophotometric analysis indicates that SN 2024jlc belongs to the class of SLSNe-Ib, characterized by low peak luminosities, distinguishable helium features, and noticeable  $^{56}\text{Ni}$  contribution. Light curves are well-fitted by both CSM-interaction and magnetar spin-down models, although the spectra do not exhibit narrow features (which would support the first mechanism) nor W-shaped features (which would support the second mechanism). Similarly to other events of the same class, a possible explanation would be that of a dense He-rich CSM region close to the star, surrounded by low-density regions. Our X-rays upper-limits are consistent with this scenario and align with previous results.

The strongest evidence in favor of a central-engine powering mechanism comes from our *Fermi*-LAT analysis. If the observed excess is real, it may point to the coexistence of multiple powering mechanisms, similarly to the case of SN 2017egm, for which spectrophotometric analyzes are suggestive of CSM interaction (Zhu et al. 2023; Lin et al. 2023), while the  $\gamma$ -ray detection supports magnetar spin-down acceleration (Acero et al. 2026).

Although yet statistically poorly populated, the SLSN-Ib class may represent a bridge between the classical SE-SNe events and SLSNe, with the key difference being the powering mechanism. The observed similarities between the two populations suggest similar progenitors in similar environments, leaving the physics behind the emission a valuable candidate for explaining the intrinsic difference between the two classes. Whether these objects are simply very luminous Type Ic or Ic-BL events remains an open question, and only future observations will shed light on this. The upcoming Vera C. Rubin Observatory's Legacy Survey of Space and Time (LSST; Ivezić et al. 2019), with its unprecedented depth and coverage, will revolutionize this field. Started in early 2026, LSST is expected to discover over 200 thousands SLSNe during the nominal 10 years of operation, offering the statistical power necessary to better understand the full diversity of SLSNe and to populate the gap between Type Ic and SLSNe. Objects like SN 2024jlc will lie in the soft spot of distance and luminosity to be precisely characterized by LSST (Simongini et al. 2025a). As the sample grows, events of this kind will be key benchmarks for understanding the physical pathways that link ordinary core collapse explosions to the most luminous stellar deaths.

*Acknowledgements.* We thank A. Segreto for his contribution in the BAT analysis and data reduction. Based on observations obtained with the Samuel Oschin Telescope 48-inch and the 60-inch Telescope at the Palomar Observatory as part of the Zwicky Transient Facility project. ZTF is supported by the National Science Foundation under Grant No. AST-2034437 and a collaboration including Caltech, IPAC, the Weizmann Institute of Science, the Oskar Klein Center at Stockholm University, the University of Maryland, Deutsches Elektronen-Synchrotron and Humboldt University, the TANGO Consortium of Taiwan, the University of Wisconsin at Milwaukee, Trinity College Dublin, Lawrence Livermore National Laboratories, and IN2P3, France. Operations are conducted by COO, IPAC, and UW. SED Machine is based upon work supported by the National Science Foundation under Grant No. 1106171 The ZTF forced-photometry service was funded under the Heising-Simons Foundation grant #12540303 (PI:

Graham). Observations reported here were obtained at the MMT Observatory, a joint facility of the Smithsonian Institution and the University of Arizona. The data presented here were obtained [in part] with ALFOSC, which is provided by the Instituto de Astrofísica de Andalucía (IAA) under a joint agreement with the University of Copenhagen and NOT. We acknowledge the use of public data from the *Swift* data archive (ID 16706, P.I. T. Moore). This research has made use of data and/or software provided by the High Energy Astrophysics Science Archive Research Center (HEASARC), which is a service of the Astrophysics Science Division at NASA/GSFC. The Pan-STARRS1 Surveys (PS1) and the PS1 public science archive have been made possible through contributions by the Institute for Astronomy, the University of Hawaii, the Pan-STARRS Project Office, the Max-Planck Society and its participating institutes, the Max Planck Institute for Astronomy, Heidelberg and the Max Planck Institute for Extraterrestrial Physics, Garching, The Johns Hopkins University, Durham University, the University of Edinburgh, the Queen's University Belfast, the Harvard-Smithsonian Center for Astrophysics, the Las Cumbres Observatory Global Telescope Network Incorporated, the National Central University of Taiwan, the Space Telescope Science Institute, the National Aeronautics and Space Administration under Grant No. NNX08AR22G issued through the Planetary Science Division of the NASA Science Mission Directorate, the National Science Foundation Grant No. AST-1238877, the University of Maryland, Eotvos Lorand University (ELTE), the Los Alamos National Laboratory, and the Gordon and Betty Moore Foundation. N.R. is funded by a Northwestern University Presidential Fellowship. N.R. is also partially supported by NSF grant # AST-2421845. Zwicky Transient Facility access for N.R. was supported by Northwestern University and the Center for Interdisciplinary Exploration and Research in Astrophysics (CIERA). This work made use of the Astro-COLIBRI platform (Reichherzer et al. 2021). FA acknowledges financial support from the Centre national d'études spatiales (CNES), France (ROR: <https://ror.org/04h1h0y33>) within the framework of the Fermi mission.

## References

- Acero, F., Acharyya, A., Adelfio, A., et al. 2026, *A&A*, 709, A229
- Acharyya, A., Adams, C., Bangale, P., et al. 2023, *ApJ*, 945, 30
- Albareti, F. D., Prieto, C. A., Almeida, A., et al. 2017, *ApJ* Supplement Series, 233, 25
- Anderson, J. P., Pessi, P. J., Dessart, L., et al. 2018, *A&A*, 620, A67
- Andreoni, I., Lu, W., Grefenstette, B., et al. 2022, *ApJ*, 941, L16
- Andrews, B. H. & Martini, P. 2013, *ApJ*, 765, 140
- Arnett, W. D. 1982, *ApJ*, 253, 785
- Atwood, W., Abdo, A. A., Ackermann, M., et al. 2009, *ApJ*, 697, 1071
- Ballet, J., Bruel, P., Burnett, T., Lott, B., et al. 2023, arXiv preprint arXiv:2307.12546
- Barbarino, C., Sollerman, J., Taddia, F., et al. 2021, *A&A*, 651, A81
- Barthelmy, S. D., Barbier, L. M., Cummings, J. R., et al. 2005, *Space Science Reviews*, 120, 143
- Bekhti, N. B., Flöer, L., Keller, R., et al. 2016, *A&A*, 594, A116
- Bellm, E. C., Kulkarni, S. R., Graham, M. J., et al. 2019, *PASP*, 131, 018002
- Bhrombhakdi, K., Chormock, R., Margutti, R., et al. 2018, *ApJ*, 868, L32
- Blagorodnova, N., Neill, J. D., Walters, R., et al. 2018, *PASP*, 130, 035003
- Blanchard, P. K., Berger, E., Gomez, S., et al. 2026, *ApJ*, 999, 59
- Breeveld, A. A., Landsman, W., Holland, S. T., et al. 2011, in *American Institute of Physics Conference Series*, Vol. 1358, *Gamma Ray Bursts 2010*, ed. J. E. McEnery, J. L. Racusin, & N. Gehrels (AIP), 373–376
- Brose, R., Sushch, I., & Mackey, J. 2022, *MNRAS*, 516, 492
- Burrows, D. N., Hill, J., Nousek, J., et al. 2005, *Space science reviews*, 120, 165
- Byler, N., Dalcanton, J. J., Conroy, C., & Johnson, B. D. 2017, *ApJ*, 840, 44
- Calzetti, D., Armus, L., Bohlin, R. C., et al. 2000, *ApJ*, 533, 682
- Chabrier, G. 2003, *PASP*, 115, 763
- Chambers, K. C., Magnier, E. A., Metcalfe, N., et al. 2016, arXiv e-prints, arXiv:1612.05560
- Chatzopoulos, E., Wheeler, J. C., Vinko, J., Horvath, Z., & Nagy, A. 2013, *ApJ*, 773, 76
- Chen, Z., Yan, L., Kangas, T., et al. 2023a, *ApJ*, 943, 41
- Chen, Z., Yan, L., Kangas, T., et al. 2023b, *ApJ*, 943, 42
- Cheung, C., Johnson, T., Jean, P., et al. 2022, *The Astrophysical Journal*, 935, 44
- Conroy, C., Gunn, J. E., & White, M. 2009, *ApJ*, 699, 486
- Coughlin, M. W., Bloom, J. S., Nir, G., et al. 2023, *ApJS*, 267, 31
- Crnogorčević, M., Linden, T., Goobar, A., & Metzger, B. D. 2026, arXiv preprint arXiv:2604.16595
- Curti, M., Cresci, G., Mannucci, F., et al. 2017, *MNRAS*, 465, 1384
- Dahiwal, A., Fremling, C., & Sharma, Y. 2019, *Transient Name Server Classification Report*, 2019-2837, 1
- De Cia, A., Gal-Yam, A., Rubin, A., et al. 2018, *ApJ*, 860, 100
- DeKany, R., Smith, R. M., Riddle, R., et al. 2020, *PASP*, 132, 038001

- Djupvik, A. A. & Andersen, J. 2010, in *Highlights of Spanish astrophysics V* (Springer), 211–218
- Eftekhari, T., Berger, E., Margalit, B., et al. 2019, *ApJ*, 876, L10
- Fabricant, D., Fata, R., Epps, H., et al. 2019, *PASP*, 131, 075004
- Fiore, A., Kozyreva, A., Yan, L., et al. 2026, arXiv preprint arXiv:2602.12948
- Flewellling, H. e., Magnier, E., Chambers, K., et al. 2020, *ApJS*, 251, 7
- Foley, R. J., Papenkov, M. S., Swift, B. J., et al. 2003, *PASP*, 115, 1220
- Foreman-Mackey, D., Sick, J., & Johnson, B. 2014, *Python-Fsps: Python Bindings To Fsps (V0.1.1)*
- Fremming, C., Sollerman, J., Taddia, F., et al. 2016, *A&A*, 593, A68
- Gal-Yam, A. 2019, *ARA&A*, 57, 305
- Gehrels, N., Chincarini, G., Giommi, P., et al. 2004, *ApJ*, 611, 1005
- Gomez, S., Berger, E., Nicholl, M., Blanchard, P. K., & Hosseinzadeh, G. 2022, *ApJ*, 941, 107
- Gomez, S., Nicholl, M., Berger, E., et al. 2024, *MNRAS*, 535, 471
- Graham, M. J., Kulkarni, S., Bellm, E. C., et al. 2019, *PASP*, 131, 078001
- Guillochon, J., Nicholl, M., Villar, V. A., et al. 2018, *ApJS*, 236, 6
- Horne, K. 1986, *PASP*, 98, 609
- Howell, D. A. 2017, in *Handbook of Supernovae* (Springer), 431–458
- Inserra, C. 2019, *Nature Astronomy*, 3, 697
- Inserra, C., Nicholl, M., Chen, T.-W., et al. 2017, *MNRAS*, 468, 4642
- Inserra, C., Smartt, S., Jerkstrand, A., et al. 2013, *ApJ*, 770, 128
- Ivezić, Ž., Kahn, S. M., Tyson, J. A., et al. 2019, *ApJ*, 873, 111
- Johnson, B. D., Leja, J., Conroy, C., & Speagle, J. S. 2021, *ApJS*, 254, 22
- Karamahmetoglu, E., Sollerman, J., Taddia, F., et al. 2023, *A&A*, 678, A87
- Kasen, D. & Bildsten, L. 2010, *ApJ*, 717, 245
- Kennicutt, Robert C., J. 1998, *ARA&A*, 36, 189
- Kim, Y.-L., Rigault, M., Neill, J., et al. 2022, *PASP*, 134, 024505
- Kumar, H., Berger, E., Blanchard, P. K., et al. 2025a, arXiv preprint arXiv:2501.01485
- Kumar, H., Berger, E., Blanchard, P. K., et al. 2025b, *ApJ*, 992, 122
- Lang, D. 2014, *AJ*, 147, 108
- Levan, A. J., Read, A., Metzger, B., Wheatley, P., & Tanvir, N. 2013, *ApJ*, 771, 136
- Li, S., Liang, Y.-F., Liao, N.-H., Lei, L., & Fan, Y.-Z. 2026, *Physical Review Letters*, 136, 111402
- Lin, W., Wang, X., Yan, L., et al. 2023, *Nature Astronomy*, 7, 779
- Madau, P. & Dickinson, M. 2014, *ARA&A*, 52, 415
- Mainzer, A., Bauer, J., Cutri, R., et al. 2014, *ApJ*, 792, 30
- Margutti, R., Bright, J., Matthews, D., et al. 2023, *ApJ*, 954, L45
- Margutti, R., Chornock, R., Metzger, B., et al. 2018, *ApJ*, 864, 45
- Margutti, R., Metzger, B., Chornock, R., et al. 2017, *ApJ*, 836, 25
- Margutti, R., Milisavljevic, D., Soderberg, A., et al. 2014, *ApJ*, 797, 107
- Margutti, R., Soderberg, A., Chomiuk, L., et al. 2012, *ApJ*, 751, 134
- Masci, F. J., Laher, R. R., Rusholme, B., et al. 2018, *PASP*, 131, 018003
- Mazzali, P., Sullivan, M., Pian, E., Greiner, J., & Kann, D. 2016, *MNRAS*, 458, 3455
- McCall, M. L. 2004, *AJ*, 128, 2144
- Meisner, A. M., Lang, D., & Schlegel, D. J. 2017, *The Astronomical Journal*, 153, 38
- Miller, J. & Stone, R. 1994, *Lick Obs. Tech. rep.*, Tech. Rep. 66. Santa Cruz: Lick Obs
- Moriya, T. J. 2024, arXiv preprint arXiv:2407.12302
- Moriya, T. J., Sorokina, E. I., & Chevalier, R. A. 2018, *Space Science Reviews*, 214, 1
- Murase, K., Kashiyama, K., Kiuchi, K., & Bartos, I. 2015, *ApJ*, 805, 82
- Murase, K., Thompson, T. A., Lacki, B. C., & Beacom, J. F. 2011, *Physical Review D—Particles, Fields, Gravitation, and Cosmology*, 84, 043003
- Nicholl, M., Berger, E., Blanchard, P. K., Gomez, S., & Chornock, R. 2019, *ApJ*, 871, 102
- Nicholl, M., Smartt, S. J., Jerkstrand, A., et al. 2015, *MNRAS*, 452, 3869
- Ofek, E., Fox, D., Cenko, S. B., et al. 2013, *ApJ*, 763, 42
- Oke, J. & Gunn, J. 1982, *PASP*, 94, 586
- Osterbrock, D. E. & Ferland, G. J. 2006, *Astrophysics of gaseous nebulae and active galactic nuclei* (University Science Books)
- Pedregosa, F., Varoquaux, G., Gramfort, A., et al. 2011, *Journal of Machine Learning Research*, 12, 2825
- Pérez-Fourmon, I., Poidevin, F., Delgado-González, Z., et al. 2024, *Transient Name Server Classification Report*, 2024-2320, 1
- Pettini, M. & Pagel, B. E. J. 2004, *MNRAS*, 348, L59
- Piascik, A., Steele, I. A., Bates, S. D., et al. 2014, in *Ground-based and Airborne Instrumentation for Astronomy V*, Vol. 9147, SPIE, 2703–2718
- Planck Collaboration, Aghanim, N., Akrami, Y., et al. 2020, *A&A*, 641, A6
- Poole, T. S., Breeveld, A. A., Page, M. J., et al. 2008, *MNRAS*, 383, 627
- Price-Whelan, A. M., Lim, P. L., Earl, N., et al. 2022, *ApJ*, 935, 167
- Prochaska, J. X., Hennawi, J. F., Westfall, K. B., et al. 2020, arXiv preprint arXiv:2005.06505
- Quimby, R. M., De Cia, A., Gal-Yam, A., et al. 2018, *ApJ*, 855, 2
- Reichherzer, P., Schüssler, F., Lefranc, V., et al. 2021, *ApJS*, 256, 5
- Renault-Tinacci, N., Kotera, K., Neronov, A., & Ando, S. 2018, *A&A*, 611, A45
- Rigault, M., Neill, J., Blagorodnova, N., et al. 2019, *A&A*, 627, A115
- Roming, P. W., Kennedy, T. E., Mason, K. O., et al. 2005, *Space Science Reviews*, 120, 95
- Sarin, N., Hübner, M., Omand, C. M., et al. 2024, *MNRAS*, 531, 1203
- Schlafly, E. F. & Finkbeiner, D. P. 2011, *ApJ*, 737, 103
- Schlegel, D. J., Finkbeiner, D. P., & Davis, M. 1998, *ApJ*, 500, 525
- Schulze, S., Yaron, O., Sollerman, J., et al. 2021, *ApJS*, 255, 29
- Schweyer, T., Sollerman, J., Jerkstrand, A., et al. 2025, *A&A*, 693, A13
- Segreto, A., Cusumano, G., Ferrigno, C., et al. 2010, *A&A*, 510, A47
- Shingles, L., Smith, K. W., Young, D. R., et al. 2021, *Transient Name Server AstroNote*, 7, 1
- Siebert, M. R., Dimitriadis, G., Polin, A., & Foley, R. J. 2020, *ApJ*, 900, L27
- Silverman, J. M., Foley, R. J., Filippenko, A. V., et al. 2012, *MNRAS*, 425, 1789
- Simongini, A., Ragosta, F., Di Palma, I., & Piranomonte, S. 2025a, *A&A*, 699, A98
- Simongini, A., Ragosta, F., Piranomonte, S., & Di Palma, I. 2024, *MNRAS*, 533, 3053
- Simongini, A., Ragosta, F., Piranomonte, S., & Di Palma, I. 2025b, *CASTOR: v2.0 - 2025-03-05*
- Smith, K., Smartt, S., Young, D., et al. 2020, *PASP*, 132, 085002
- Sollerman, J., Fremming, C., Perley, D., & Laz, T. D. 2024, *Transient Name Server Discovery Report*, 2024-1681, 1
- Speagle, J. S. 2020, *MNRAS*, 493, 3132
- Steele, I. A., Smith, R. J., Rees, P. C., et al. 2004, in *Ground-based Telescopes*, Vol. 5489, SPIE, 679–692
- Taddia, F., Sollerman, J., Fremming, C., et al. 2019, *A&A*, 621, A71
- Taddia, F., Sollerman, J., Leloudas, G., et al. 2015, *A&A*, 574, A60
- Terreran, G., Blanchard, P., DeMarchi, L., et al. 2020, *The Astronomer's Telegram*, 13970, 1
- Thornton, I., Villar, V. A., Gomez, S., & Hosseinzadeh, G. 2024, *villrv/extrabool: RNAAS Release*
- Tinyanont, S., Woosley, S. E., Taggart, K., et al. 2023, *ApJ*, 951, 34
- Tonry, J., Denneau, L., Heinze, A., et al. 2018, *PASP*, 130, 064505
- Van Der Walt, S., Colbert, S. C., & Varoquaux, G. 2011, *Computing in science & engineering*, 13, 22
- van der Walt, S. J., Crellin-Quick, A., & Bloom, J. S. 2019, *Journal of Open Source Software*, 4, 1247
- Van Dokkum, P. G. 2001, *PASP*, 113, 1420
- Virtanen, P., Gommers, R., Oliphant, T. E., et al. 2020, *Nature methods*, 17, 261
- Vurm, I. & Metzger, B. D. 2021, *The Astrophysical Journal*, 917, 77
- Wheeler, J. C., Chatzopoulos, E., Vinkó, J., & Tuminello, R. 2017, *ApJ*, 851, L14
- Wise, J., Hinds, K., Perley, D., et al. 2024, *Transient Name Server AstroNote*, 193, 1
- Wood, M., Caputo, R., Charles, E., et al. 2018, *Fermipy: Fermi-LAT data analysis package*, *Astrophysics Source Code Library*, record ascl:1812.006
- Wright, A. H., Robotham, A. S. G., Bourne, N., et al. 2016, *MNRAS*, 460, 765
- Wright, E. L., Eisenhardt, P. R. M., Mainzer, A. K., et al. 2010, *AJ*, 140, 1868
- Yan, L., Perley, D., Schulze, S., et al. 2020, *ApJ*, 902, L8
- Zhu, J., Jiang, N., Dong, S., et al. 2023, *ApJ*, 949, 23

<sup>1</sup> INAF - Osservatorio Astronomico di Roma, Via di Frascati 33, I-00078 Monteporzio Catone, Italy

<sup>2</sup> Università Tor Vergata, Dipartimento di Fisica, Via della Ricerca Scientifica 1, I-00133 Rome, Italy

<sup>3</sup> FSLAC IRL 2009, CNRS/IAC, La Laguna, Tenerife, Spain

<sup>4</sup> Université Paris-Saclay, Université Paris Cité, CEA, CNRS, AIM, 91191 Gif-sur-Yvette, France

<sup>5</sup> Institute of Space Sciences (ICE, CSIC), Campus UAB, Carrer de Can Magrans s/n, E-08193 Barcelona, Spain

<sup>6</sup> Institut d'Estudis Espacials de Catalunya (IEEC), E-08860 Castelldefels (Barcelona), Spain

<sup>7</sup> Astrophysics Research Institute, Liverpool John Moores University, 146 Brownlow Hill, Liverpool L3 5RF, UK

<sup>8</sup> The Oskar Klein Centre, Department of Astronomy, AlbaNova, SE-106 91 Stockholm, Sweden

<sup>9</sup> Center for Interdisciplinary Exploration and Research in Astrophysics (CIERA), 1800 Sherman Avenue, Evanston, IL 60201, USA

<sup>10</sup> University College London, Mullard Space Science Laboratory, Holmbury St. Mary, Dorking, RH5 6NT, U.K.

<sup>11</sup> IPAC, California Institute of Technology, 1200 E. California Blvd, Pasadena, CA 91125, USA

<sup>12</sup> Caltech Optical Observatories, California Institute of Technology, Pasadena, CA 91125, USA

- <sup>13</sup> Division of Physics, Mathematics and Astronomy, California Institute of Technology, 1200 E. California Blvd, Pasadena, CA 91125, USA
- <sup>14</sup> Nordic Optical Telescope, Rambla José Ana Fernández Pérez 7, ES-38711 Breña Baja, Spain
- <sup>15</sup> Department of Physics and Astronomy, Northwestern University, 2145 Sheridan Road, Evanston, IL 60208, USA
- <sup>16</sup> NSF-Simons AI Institute for the Sky (SkAI), 172 E. Chestnut St., Chicago, IL 60611, USA
- <sup>17</sup> Department of Physics & Astronomy, University of California Los Angeles, 430 Portola Plaza, Los Angeles, CA 90095-1547, US

## Appendix A: Tables and Data

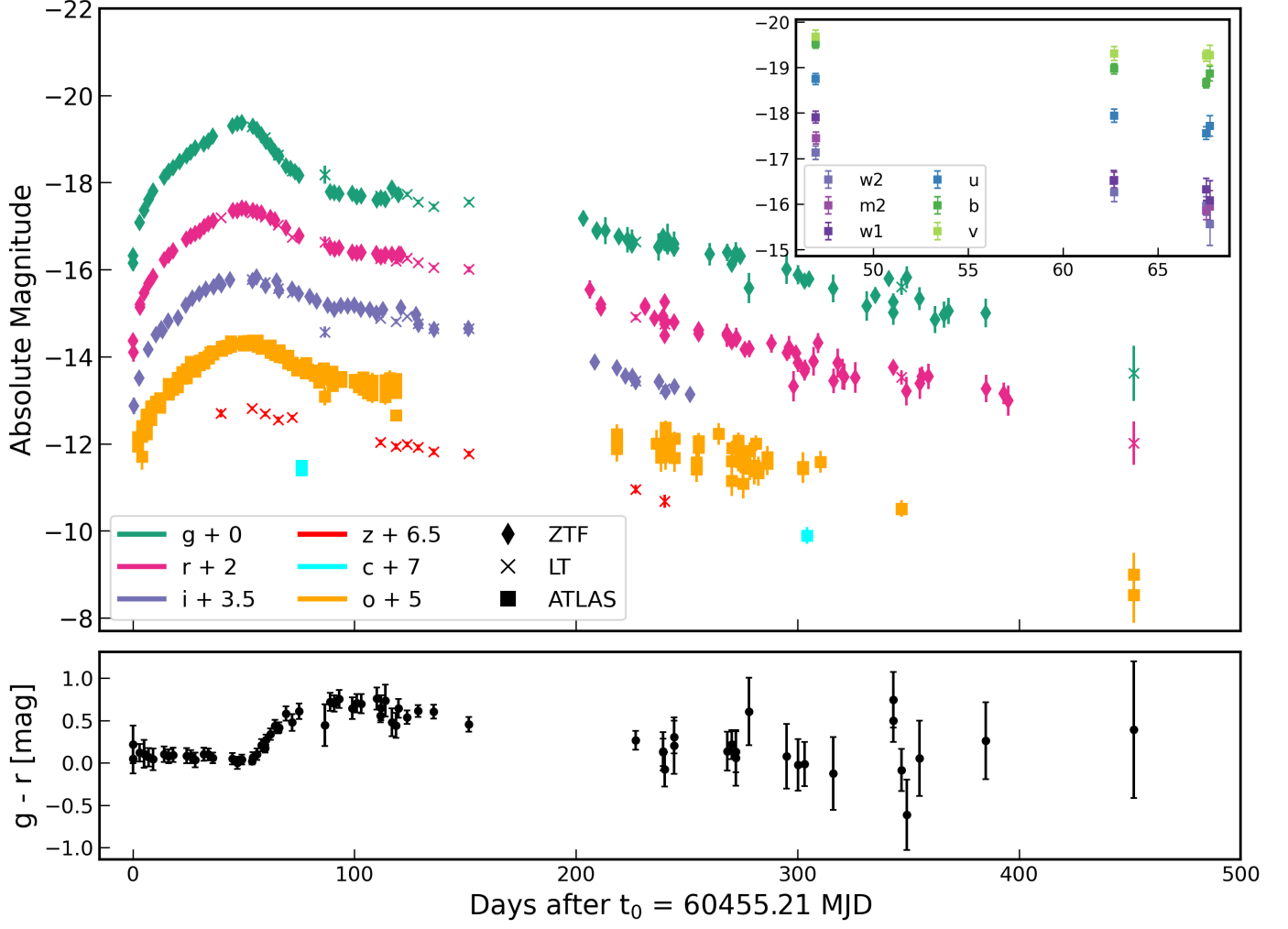


**Fig. A.1.** Photometry of SN 2024jlc. All bands are in the AB system and presented since the time of explosion  $t_0$ . The main panel shows the optical evolution of the  $griz$  and  $c$  and  $o$  bands over the first 450 days. The insert panel shows the *Swift*-UVOT filters across the three observation epochs. The lower panel shows the  $g - r$  color evolution over the same time range. Data are reported in Table A.2.

**Table A.1.** Measurements of host-galaxy brightness.

Source	Band	Brightness (mag, AB)
PanSTARRS	$g$	$17.78 \pm 0.03$
PanSTARRS	$i$	$17.27 \pm 0.07$
PanSTARRS	$r$	$17.36 \pm 0.03$
PanSTARRS	$z$	$17.16 \pm 0.07$
unWISE	W1	$17.88 \pm 0.09$
unWISE	W2	$18.57 \pm 0.13$

**Notes.** Not corrected for MW extinction.

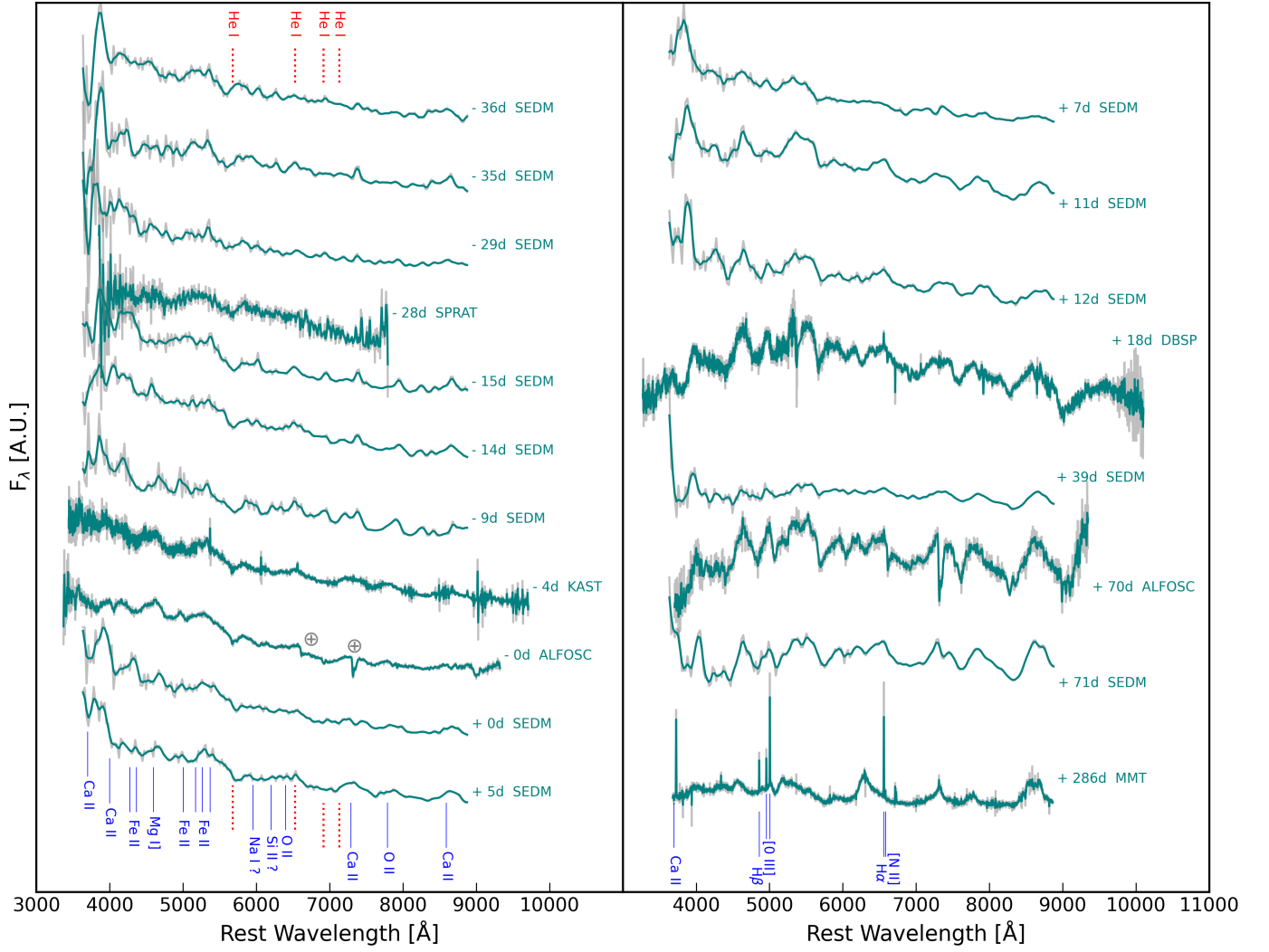


**Fig. A.2.** Spectral data of SN 2024jlc. Epochs are given with respect to the  $g$ -band time of maximum  $t_{max}$ . Fluxes are normalized and offset for better visualization. Original spectra are plotted in light gray in the background, while the smoothed interpolated spectra are shown in teal. Wavelengths are in rest-frame. We highlight some spectral features. The spectra at  $t_0 + 20.81$  d,  $t_0 + 35.75$  d, and  $t_0 + 213.34$  d are not shown due to low signal to noise ratio. Data are available on WISeREP.

**Table A.2.** Photometric data of SN 2024jlc.

Date MJD	Phase day	Mag AB	Err AB	Band	Instrument
60455.21	0.0	20.16	0.1	g	ZTF
60455.27	0.06	20.32	0.17	g	ZTF
60455.29	0.08	20.03	0.14	r	ZTF
60455.39	0.18	20.3	0.21	r	ZTF
60455.59	0.39	19.98	0.19	i	ZTF
60457.41	2.21	19.35	0.27	o	ATLAS
60457.42	2.21	19.43	0.26	o	ATLAS
60457.42	2.22	19.22	0.22	o	ATLAS
60458.09	2.89	19.34	0.09	i	ZTF
60458.26	3.05	19.39	0.1	g	ZTF
60458.37	3.16	19.2	0.03	r	ZTF
60458.37	3.16	19.26	0.11	r	ZTF
60459.39	4.18	19.02	0.14	o	ATLAS
60459.39	4.19	19.22	0.19	o	ATLAS
60459.4	4.19	19.68	0.3	o	ATLAS
60459.41	4.2	18.97	0.13	o	ATLAS
60460.28	5.07	18.93	0.12	r	ZTF
60460.31	5.1	19.11	0.11	g	ZTF
60460.31	5.1	19.11	0.11	g	ZTF
60461.4	6.2	18.87	0.12	o	ATLAS
60461.4	6.2	18.87	0.12	o	ATLAS
60461.41	6.2	18.99	0.17	o	ATLAS
60461.41	6.2	19.01	0.16	o	ATLAS
60461.41	6.2	18.74	0.12	o	ATLAS
60461.41	6.2	18.83	0.13	o	ATLAS
60461.41	6.2	18.88	0.17	o	ATLAS
60461.41	6.2	18.87	0.16	o	ATLAS
60461.41	6.21	18.81	0.15	o	ATLAS
60461.41	6.21	18.76	0.13	o	ATLAS
60461.42	6.21	19.12	0.18	o	ATLAS
60461.42	6.21	19.11	0.15	o	ATLAS
60461.42	6.21	19.16	0.16	o	ATLAS
60461.45	6.24	18.73	0.11	o	ATLAS
60461.45	6.24	18.71	0.09	o	ATLAS
60462.09	6.89	18.68	0.03	i	ZTF

**Notes.** Phases are expressed relative to  $t_0 = 60455.21$  MJD. Magnitudes are in the AB system. The full table is given as extra online material

**Table A.3.** Log of spectral observations.

Date MJD	Phase (day)	$\lambda_{\min}$ (Å)	$\lambda_{\max}$ (Å)	Exposure time (s)	Instrument	Telescope
60468.328	13.12	3776	9223	2700.0	SEDM	P60
60469.328	14.12	3776	9223	2700.0	SEDM	P60
60475.415	20.21	3776	9223	2700.0	SEDM	P60
60476.02	20.81	4002	8098	1700.0	SPRAT	LT
60489.328	34.12	3776	9223	2160.0	SEDM	P60
60490.181	34.98	3776	9223	2160.0	SEDM	P60
60490.952	35.75	4002	8097	2000.0	SPRAT	LT
60495.275	40.07	3776	9223	2160.0	SEDM	P60
60500.202	45.0	3574	10091	600	KAST	Lick-3m
60503.918	48.71	3501	9688	1200.0	ALFOSC	NOT
60505.219	50.01	3776	9223	2160.0	SEDM	P60
60510.283	55.08	3776	9223	2160.0	SEDM	P60
60512.255	57.05	3776	9223	2160.0	SEDM	P60
60516.173	60.97	3776	9223	2160.0	SEDM	P60
60517.285	62.08	3776	9223	2160.0	SEDM	P60
60523.264	68.06	3400	10498	600	DBSP	P200
60544.232	89.03	3776	9223	2160.0	SEDM	P60
60574.91	119.7	3850	9712	900.0	ALFOSC	NOT
60576.12	120.91	3776	9223	2160.0	SEDM	P60
60668.546	213.34	3776	9223	414.0	SEDM	P60
60791.389	336.18	3824	9212	1200	BINOSPEC	MMT
60791.39	336.18	3824	9212	1200	BINOSPEC	MMT

**Notes.** Phases are expressed with respect to the time of explosion  $t_0$  in the observed frame.

**Table A.4.** *Swift*-XRT observations.

Date MJD	Counts $10^{-3}$ (cts s $^{-1}$ )	Flux $10^{-13}$ (erg cm $^{-2}$ s $^{-1}$ )	Luminosity $10^{41}$ (erg s $^{-1}$ )	Exposure (s)
60502	14.7	5.076	20.33	770
60517	4.53	1.564	6.27	1910
60522	5.10	1.761	7.05	2200
—	$\leq 2.43$	$\leq 0.839$	$\leq 3.36$	4880

**Notes.** Count rates, fluxes and luminosities are  $3\sigma$  upper limits. We refer to flux as the absorbed flux, while the luminosity is obtained from the unabsorbed flux. The last line is obtained by integrating over the entire time period.

**Table A.5.** Input and output parameters for the `csnmi` model from MOSFiT

Parameter	Prior range	Prior type	Posterior
$t_{\text{exp}}$ (d)	[-10, 0]	Uniform	$-3.66^{+0.19}_{-0.22}$
$M_{\text{ej}}(M_{\odot})$	[0.1, 30]	Uniform	$8.24^{+0.83}_{-0.56}$
$M_{\text{cm}}(M_{\odot})$	[0.1, 50]	Uniform	$1.81^{+0.08}_{-0.21}$
$f_{\text{Ni}}$	$[10^{-3}, 1]$	Log-uniform	$0.17^{+0.01}_{-0.01}$
$T_{\text{min}}$ ( $10^3$ K)	[6, 20]	Uniform	$6.73^{+0.13}_{-0.06}$
$E_k$ ( $10^{51}$ erg)	[1, 10]	Log-uniform	$1.14^{+0.01}_{-0.01}$
$\sigma$	$[10^{-5}, 10]$	Log-uniform	$0.17^{+0.01}_{-0.01}$
$\rho$ ( $10^{-12}$ g cm $^{-3}$ )	$[10^{-2}, 10]$	Log-uniform	$4.49^{+1.50}_{-1.50}$
$r_0$	[1, 10]	Uniform	$9.8^{+0.98}_{-0.95}$
$n_{\text{H, host}}$ ( $10^{20}$ cm $^{-3}$ )	$[10^{-2}, 10]$	Log-uniform	$9.72^{+0.52}_{-0.23}$
$\kappa_{\gamma}$ ( $10^2$ cm $^2$ g $^{-1}$ )	$[0.1, 10^4]$	Log-uniform	$5.8^{+1.5}_{-0.5}$

**Notes.** The fit was executed giving as input redshift, Galactic extinction, luminosity distance, and number of iterations.

**Table A.6.** Input and output parameters for the `s1snmi` model from MOSFiT

Parameter	Prior range	Prior type	Posterior
$t_{\text{exp}}$ (d)	[-10, 0]	Uniform	$-5.16^{+0.78}_{-0.37}$
$M_{\text{ej}}(M_{\odot})$	[1, 30]	Uniform	$8.47^{+1.39}_{-1.14}$
$P_{\text{spin}}$ (ms)	[1, 30]	Uniform	$5.22^{+0.38}_{-0.69}$
$B$ ( $10^{14}$ G)	[1, 30]	Uniform	$2.09^{+0.50}_{-0.37}$
$f_{\text{Ni}}$	$[10^{-3}, 1]$	Log-uniform	$0.15^{+0.03}_{-0.04}$
$T_{\text{min}}$ ( $10^3$ K)	[5, 15]	Uniform	$7.3^{+0.29}_{-0.20}$
$\sigma$	$[10^{-3}, 100]$	Log-uniform	$0.16^{+0.01}_{-0.01}$
$M_{\text{NS}}(M_{\odot})$	[1, 2]	Uniform	$1.02^{+0.03}_{-0.01}$
$\alpha$	[0, 5]	Uniform	$0.17^{+1.61}_{-0.13}$
$\kappa$ (cm $^2$ g $^{-1}$ )	[0.01, 0.2]	Uniform	$0.11^{+0.01}_{-0.02}$
$\kappa_{\gamma}$ ( $10^3$ cm $^2$ g $^{-1}$ )	$[0.1, 10^4]$	Log-uniform	$4.49^{+2.34}_{-1.78}$
$v_{\text{ej}}$ ( $10^3$ km s $^{-1}$ )	[5, 13]	Uniform	$5.38^{+0.21}_{-0.23}$
$\theta_{\text{PB}}$	[0, 1.57]	Uniform	$1.12^{+0.32}_{-0.27}$
$\lambda_{\text{cutoff}}$ ( $10^3$ )	[2, 8]	Uniform	$3.57^{+4.19}_{-1.29}$
$n_{\text{H, host}}$ ( $10^{20}$ cm $^{-3}$ )	$[10^{-2}, 10]$	Log-uniform	$9.49^{+0.38}_{-1.28}$

**Notes.** The fit was executed giving as input redshift, Galactic extinction, luminosity distance, and number of iterations.

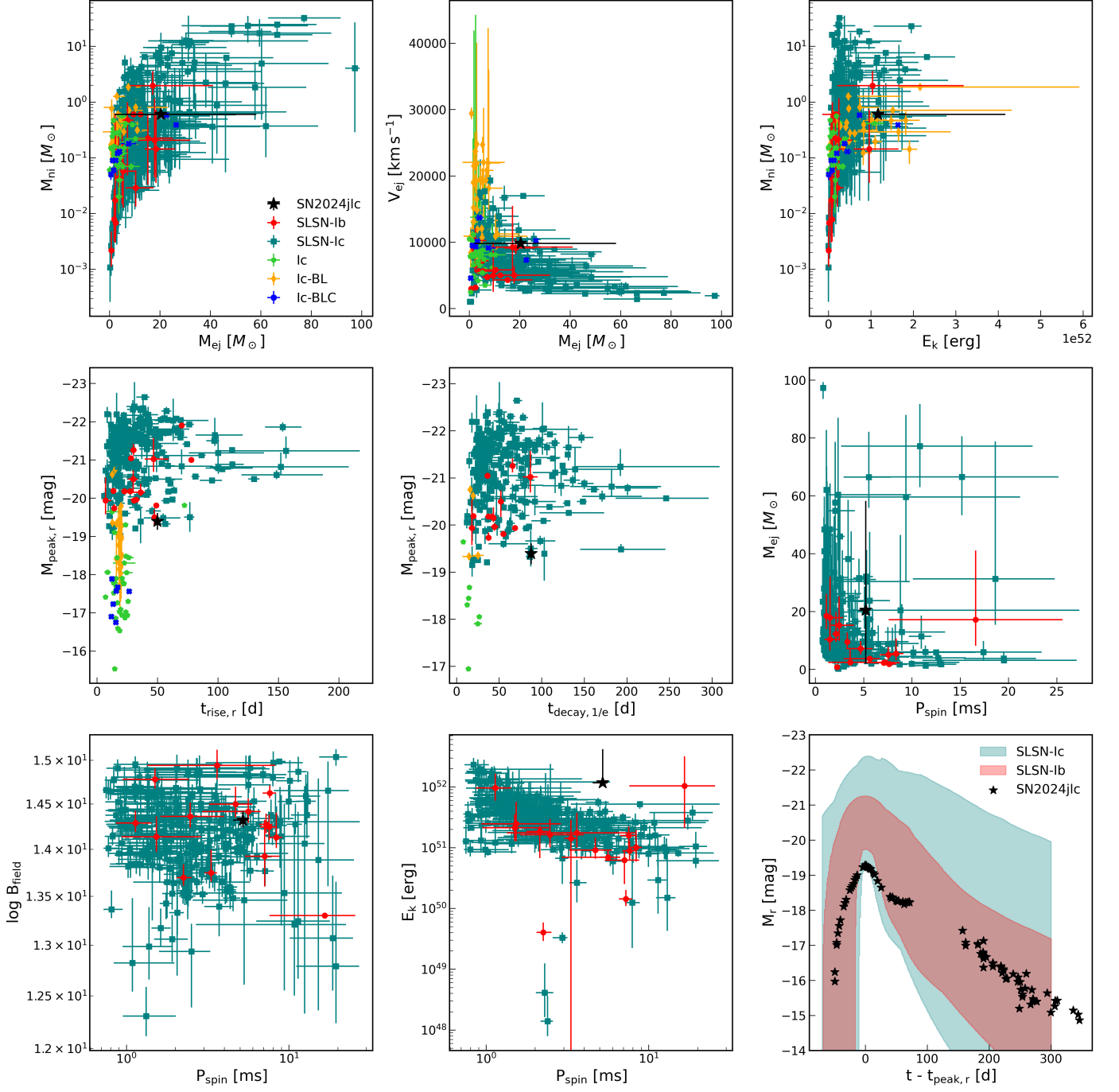


**Fig. A.3.** Comparison between SN 2024jlc parameters (black star) and SLSN-Ic (teal), SLSN-Ib (red), Ic (green), Ic-BL (orange), and Ic with broad light curves (Ic-BLC, blue) samples. SLSNe data are taken from the `s1sne` library (Gomez et al. 2024). Additional data for the SLSN-Ib sample are extracted from Gomez et al. (2022), Kumar et al. (2025b), Kumar et al. (2025a). Type Ic-BL data are taken from Taddia et al. (2015, 2019). Type Ic data are taken from Taddia et al. (2015); Barbarino et al. (2021). Type Ic-BLC are taken from Barbarino et al. (2021); Karamahmetoglu et al. (2023). Additional notes: i. the rise time ( $t_{\text{rise},r}$ ) and the peak magnitude ( $M_{\text{peak},r}$ ) are defined relative to the r-band; ii. the velocity of ejecta  $v_{\text{ej}}$  is taken as the expansion velocity relative to the maximum light; in some cases, this is a direct result of MOSFIT; iii. when missing, the kinetic energy ( $E_{\text{k}}$ ) or the velocity of the ejecta are derived from Arnett’s formula (Arnett 1982); iv. as in (Chen et al. 2023a), iPTF12gty (Barbarino et al. 2021) and iPTF15eov (Taddia et al. 2019) are included in the SLSN-Ic class.